Whole brain resting-state EEG dynamic: A mixture of linear aperiodic and nonlinear resonant stochastic processes

Ying Wang[a], Min Li[b], Ronaldo García Reyes[a,c], Deirel Paz-Linares[a,c], Jorge F. Bosch-Bayard[c,e], Maria L. Bringas-Vega[a,c], Ludovico Minati[a,d], Pedro A. Valdes-Sosa[a,c]

[a] *The Clinical Hospital of Chengdu Brain Science Institute, MOE Key Lab for NeuroInformation, University of Electronic Science and Technology of China, No. 2006, Xiyuan Ave., West Hi-Tech Zone, Chengdu, 611731, China*

[b] *Hangzhou Dianzi University, Hangzhou, Zhejiang, China*

[c] *Cuban Neuroscience Center, Havana, Cuba*

[d] *Center for Mind/Brain Sciences (CIMeC), University of Trento, 38123 Trento, Italy*

[e] *Department of Biological and Health Psychology, Faculty of Psychology, Universidad Autónoma de Madrid, Spain*

Abstract

Parameterizing electroencephalography (EEG) signals in the spectral domain reveals physiologically relevant components of neural stochastic processes, yet the linearity or nonlinearity of these components remains debated and could not solved by the current Spectral Parameter Analysis (SPA). We address this using BiSCA (**BiS**pectral EEG **C**omponent **A**nalysis), a likelihood-based model unifies EEG spectrum and bispectrum analysis to identify inter-frequency harmonic relationships and distinguish signal components. Simulations demonstrate BiSCA's ability to separate nonlinearity from non-Gaussianity (e.g., linear non-Gaussian systems exhibit diffuse bicoherence, while nonlinear Gaussian systems show localized peaks). Analyzing 1,771 intracranial EEG (iEEG) channels and 960 subjects HarMNqEEG dataset, we uncover a clear organizational principle: the brain's aperiodic (ξ) activity is predominantly linear, whereas its resonant (ρ) oscillations, including Alpha (α) rhythms and other peaks, are the primary source of cortical quadratic nonlinearity. This finding challenges the long-held notion of widespread linearity in large-scale brain signals, as our analysis reveals that over two-thirds of EEG and iEEG channels exhibit significant nonlinear characteristics. Spatially, we uncover a striking dissociation between signal power and nonlinearity: while the occipital Alpha (α) rhythm dominates in power, the parietal Mu (μ) rhythm generates the strongest nonlinear signature. These findings highlight that nonlinearity is present across the brain, arising from resonant activity.

Highlights

New Spectral domain Model (BiSCA): A novel model, BiSCA, which extends the phase blind SPA methods to third-order cumulant spectrum, is presented that jointly analyzes the spectrum and bispectrum, available to parametrize nonlinear EEG components in the spectral domain.

Challenges Linear Brain Models: The findings show that significant nonlinearities exist in whole-brain EEG, challenging the idea that these complex dynamics are averaged at large scales.

Identifies Distinct EEG Component Roles: The study reveals that the aperiodic (Xi) signal component is linear, while resonant rhythms (Rho), like Alpha and Mu, are the primary source of nonlinearity.

Brain Nonlinearity across modality: Analysis of extensive rs-EEG (960 subjects, 18 channels for each subject) and rs-iEEG data(105 subjects, total 1771 electrodes) confirms that the observation process of volume conduction does not decay nonlinearity.

Separates Nonlinearity from Non-Gaussianity: The method successfully distinguishes between true system nonlinearity and statistical non-Gaussianity, a crucial separation for accurate modeling.

Maps Spatial Patterns of Nonlinearity: The research identifies distinct topographic maps of nonlinearity, linking more substantial effects to specific brain regions and rhythms like the Mu rhythm in the parietal lobe.

1. Introduction

A pivotal debate in neuroscience centers on whether mesoscale brain dynamics, as reflected in resting state EEG (rsEEG) and fMRI (rsfMRI), can be described entirely as linear, Gaussian stochastic processes. Recent studies, such as Nozari et al. (2024) and Raffaelli et al. (2024), argue that linear time series models suffice, suggesting that the intricate nonlinearities observed at the microscale—within neurons, synapses, and neural masses—are effectively "averaged out" at larger scales. This hypothesis carries profound implications: if true, it would imply that mesoscale signals lack observable nonlinear signatures, limiting our ability to infer microscale dynamics from macroscopic measurements.

Given the high temporal resolution of the scalp or intracranial resting-state EEG (rsEEG) (Figure 1a), which makes it particularly suitable for investigating dynamic neural processes, reports asserting linearity or Gaussianity are somewhat surprising science substantial evidence indicates that nonlinear dynamics are observable in rsEEG signals. Nonlinear dynamics in neural systems, as evidenced by phenomena in the frequency domain such as nonlinear resonance, cross-frequency coupling (CFC), and phase-amplitude coupling (PAC), are critical for understanding the complex oscillatory interactions observed in resting-state EEG (rsEEG) and task-related EEG signals. Nonlinear resonance phenomena in neural systems were first systematically described by Lopes da Silva et al., (1976), who demonstrated cross-frequency coupling of the iEEG from the visual cortex of dogs using bicoherence, a normalized third-order spectrum (bispectrum). This pioneering work established the foundation for understanding nonlinear resonance in neural systems and supported their nonlinear neural mass model. Van Albada & Robinson (2013) demonstrated strong harmonic relations for the rhythms in the rsEEG data from 1424 healthy subjects, further confirming nonlinear resonance mechanisms, discussing the nonlinear neural field model describing the phenomenon. Further evidence of cross-nonlinearities emerges in task-related EEG data, such as steady-state visual evoked potentials (SSVEP) (Roberts & Robinson, 2012; Labecki et al., 2016), motor tasks (Sheremet et al., 2016), decision-making and memory tasks (Klimesch, 2012), and seizure activity (Mohsini et al., 2017). Subsequent theoretical and empirical work by Nolte and colleagues demonstrated the mathematical equivalence between phase-amplitude coupling measures and bispectral analysis, providing a unified framework for understanding nonlinear resonance in neural systems (Zandvoort & Nolte, 2021). Furthermore, large-scale brain network models have shown that cross-frequency coupling emerges naturally from the nonlinear dynamics of interconnected neural populations, supporting the view that nonlinear resonance is a fundamental organizing principle of brain activity (Jirsa & Müller, 2013). Critically, if macroscopic signals were limited to low-order statistical properties (e.g., mean, variance), none of these nonlinear resonance phenomena would have been observed, then widely and successfully used techniques like Independent Component Analysis (ICA) — which relies on higher-order moments—would fail to separate signal sources.

This debate can be resolved by recognizing that various neural phenomena - including phase coupling, intermodulation, and harmonic generation - can be unified under the theoretical framework of nonlinear resonance. Nonlinear resonance comprehensively explains the complex dynamics observed in neural systems, bridging the gap between microscale nonlinearities and macroscale observations.

This debate is obfuscated by ignoring a critical distinction between linearity—the functional form of a system's temporal evolution, governed by superposition—and Gaussianity—the statistical distribution of its variables. A linear system, such as an autoregressive model, can yield non-Gaussian outputs if driven by non-Gaussian inputs (e.g., skewed or heavy-tailed noise). Conversely, a nonlinear system may produce approximately Gaussian statistics when nonlinear effects are subtle or mimic the summation of many independent components, approximating a Central Limit Theorem scenario. However, strongly nonlinear systems frequently exhibit pronounced non-Gaussianity, such as multimodal or skewed distributions—especially when involving harmonic coupling or multiplicative feedback. Thus, neural dynamics can embody any combination of linearity/nonlinearity and Gaussianity/non-Gaussianity, necessitating careful separation of these concepts in EEG analysis.

It is also important to recognize that the EEG signal is a mixture of different types of processes and that Gaussianity or linearity (or their absence) may vary across these processes. Understanding the differential properties of distinct EEG components is crucial to our analysis, as it allows for a more nuanced interpretation of the underlying neural mechanisms. By dissecting the contributions of various subprocesses—such as oscillatory rhythms, aperiodic activity, and noise—it becomes possible to identify which components adhere to linear dynamics and Gaussian statistics and which deviate due to nonlinear interactions or non-Gaussian inputs. This component-specific approach not only refines our understanding of EEG generation but also enhances the accuracy of macroscale models in capturing microscale dynamics.

One very successful strand of research for decomposing the EEG into processes is based on the EEG second-order cumulant $S(f)$ or spectrum for frequency f. This is a logical choice since, for strictly stationary processes without long-term memory (Brillinger), the distribution of optimized estimators $\hat{S}(f)$ (for example, with Multitapers) and completely characterizes linear time-invariant signals driven by noise. Figure 1b illustrates the separation of an EEG $\hat{S}(f)$ into distinct components defined by simple functional forms, each determined by only a few parameters, an approach known as **Spectral Parameter Analysis** (**SPA**) (Appendix A.2). An early example of SPA is Pascual-Marqui et al. (1987), who proposed the Xi-Alpha (ξα) model. They showed that EEG spectra have two dominant components: an aperiodic (Xi, ξ) component and multiple peaks characterizing rhythmic activity (which we will call generically Rho components or ρ), the best known being the Alpha (α) component (the Peak 1 in Figure 1b). The FOOOF model is a recent example of SPA (Donoghue et al., 2020). Not only do these components have

important behavioral correlates (Connor, 2022; Dragovic et al., 2022; McKeon et al., 2024), but they also ignited research into their distinctive physiological underpinning (Brake et al., 2024; Kramer & Chu, 2024).

However, SPA is only optimal for characterizing linear Gaussian systems. Higher-order moments vanish for this type of system, and second-order moments suffice. Unfortunately, SPA is thus blind to nonlinear dynamics. For this type of activity, higher-order spectral tools, such as the bispectrum $B(f_1, f_2)$ and its normalized version, the bicoherence $b\left(f_1, f_2\right)$, between frequencies f_1 and f_2 , are required to detect phenomena like harmonic generation, phase coupling, or other nonlinear interactions. Notably, this underscores that only testing the marginal Gaussianity of a signal is insufficient to detect nonlinearity since many nonlinear systems can generate marginal distributions indistinguishable from Gaussian. Analysis of nonlinear time series (multiple lags) is needed. Another fundamental problem of state-of-the-art SPA is that the harmonic relationships between second-order spectral peaks are not explicitly modeled despite their being ubiquitous in EEG recordings.

We introduce BiSCA (**BiS**pectral EEG **C**omponent **A**nalysis), a generalized model of EEG spectral components designed to detect and quantify nonlinear resonance and address the limitations of current spectral analysis models. Unlike traditional approaches focusing solely on isolated second-order spectral peaks, which is phase blind, BiSCA provides a combined model specifically designed to identify nonlinear resonance phenomena in neural signals, allows modeling harmonically related second-order peaks and their corresponding bispectral counterparts. This extension allows for a more comprehensive characterization of EEG activity. Furthermore, BiSCA parameter estimation is based on maximum likelihood, enabling direct statistical testing of linearity and Gaussianity for each component. We show these components for one case in (Figure 1 e-g). We note that the present version of the model is for a "quasi-stationary" EEG time series. A time-resolved BiSCA in the spirit of (Wilson et al., 2022a) is a straightforward work in progress.

In the second part of our paper, we demonstrate how the BISCA model reveals substantial nonlinearities and non-Gaussian characteristics in EEG data using 1,771 resting-state intracranial EEG (iEEG) recordings from 106 patients. In contrast to the hypothesis that such nonlinearities are averaged out in the coarser scalp recordings, we show this is not the case using 1,391 EEG resting-state scalp (rsEEG) recordings from healthy participants.

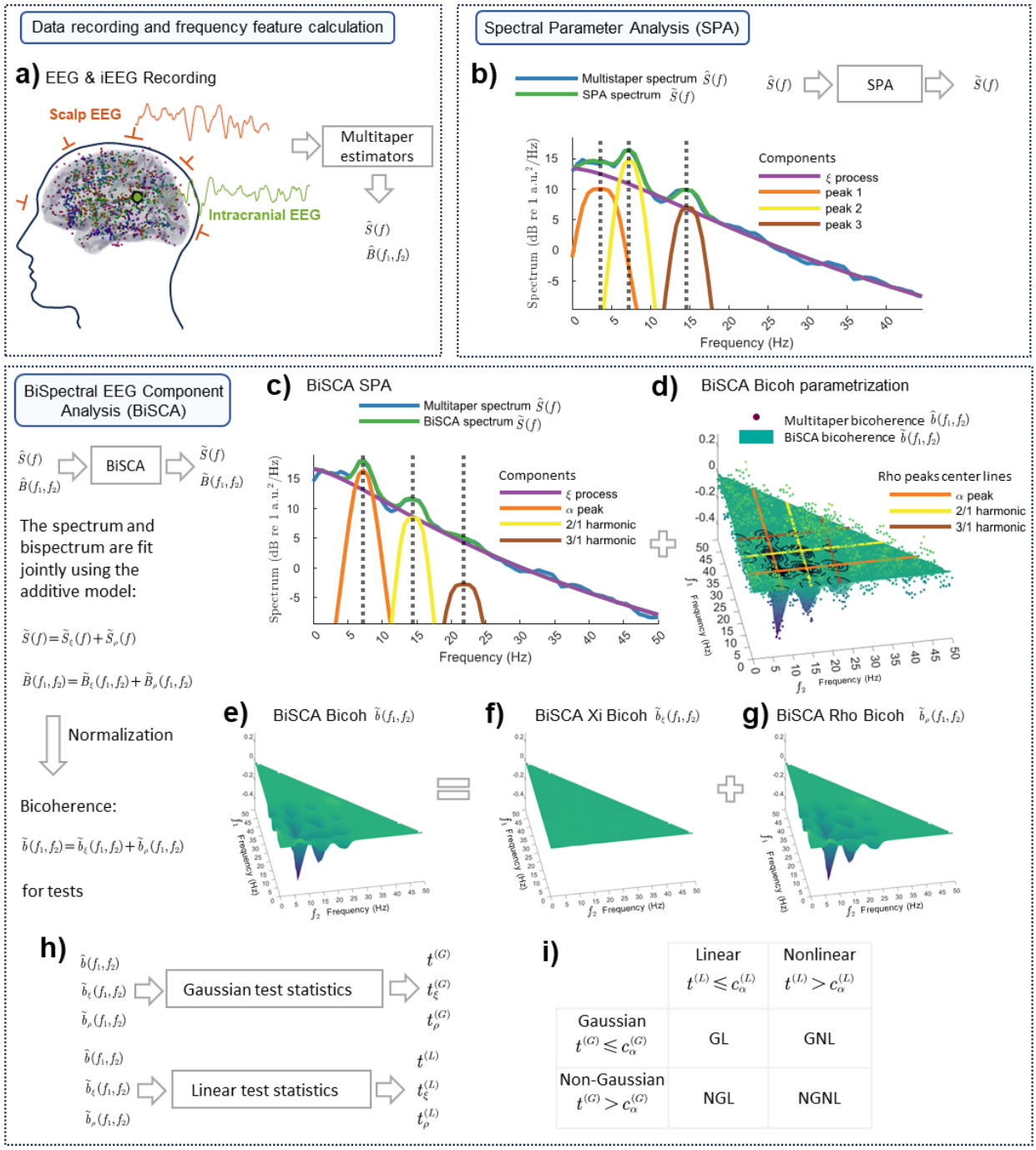

Figure 1: Uncovering rsEEG nonlinearity and non-Gaussianity with BiSCA (BiSpectral Components Analysis)*. (a) We obtain for intracranial EEG (iEEG) and resting state EEG the Multitaper Spectral and Bispectral Estimators, $\hat{S}(f)$ and $\hat{B}(f_1, f_2)$ which are data summaries. (b) SPA (Spectral Parameter Analysis) decomposes $\hat{S}(f)$ as a linear superposition of individual peaks (color-coded lines) to produce a SPA model spectrum $\tilde{S}(f)$. The BiSCA model (c)-(g) designed to parametrize nonlinear resonances through joint modeling spectrum and bispectrum($\hat{S}(f)$ $\hat{B}(f_1, f_2)$) analysis to producing BiSCA spectral and bispectral estimators $\tilde{S}(f)$ and $\tilde{B}(f_{1,2})$; (c) Spectral data $\hat{S}(f)$ and BiSCA $\tilde{S}(f)$ fits that model harmonic relationships; (d) Data of the Real part of the bicoherence $\hat{b}(f_1, f_2)$ and BiSCA model fits $\tilde{b}(f_1, f_2)$. Bicoherence is the normalized version of the bispectrum. Lines for the*

harmonics shown in (c) are superimposed on the f_1-f_2 plane are Additive decomposition of BiSCA bicoherence (e-f), with (e) total bicoherence, (f) bicoherence of Xi-component, and (g) bicoherence of Rho-component; In (h), these bicoherence used to calculate the statistic for the non-Gaussian and nonlinear test; (i) the table classifies the signal by comparing to the critical value of Gaussianity and Linearity test, a signal is classified as Gaussian if $t^{(G)} \leq c_\alpha^{(G)}$ and Linear if $t^{(L)} \leq c_\alpha^{(L)}$; otherwise, it is classified as Non-Gaussian or Nonlinear, respectively.

2. Results

2.1 Nonlinear and non-Gaussian cortical dynamics in EEG/iEEG revealed by Bicoherence.

We assessed linearity and Gaussianity for the quasi-stationary EEG and iEEG data using the modified Hinich test (Hinich, 1982) based on the Multitaper Bicoherence $\hat{b}(f_1, f_2)$, with a threshold adjusted using the Benjamini-Hochberg FDR procedure (q=0.001). The results of these tests are presented in Table 1, classified as depicted in Figure 1i. Note that our reference to linearity or Gaussianity indicates the rejection of the null hypothesis in the corresponding tests. Despite the conservative value for q, only 14.7% of the EEG and 25.7% of the iEEG recordings tested linear and Gaussian. It is noteworthy that 81.6% of EEGs and 67.9% of iEEG recordings were either nonlinear or non-Gaussian. Very few recordings tested as linear and non-Gaussian: 3.6% for EEG and 6.4% for iEEG, respectively. The proportions of Gaussianity and non-Gaussianity for nonlinear recordings were approximately the same for both EEG and iEEG. A detailed breakdown of the test statistics from different perspectives is provided in Figure 2.

Table 1 Percentages of EEG and iEEG recordings that are Linear, Nonlinear, Gaussian or non-Gaussian

	EEG			**iEEG**		
	Linear	Nonlinear	Total	Linear	Nonlinear	Total
Gaussian	14.7	39.3	54	25.7	17.1	42.7
Non-Gaussian	3.6	42.3	46	6.4	50.9	57.3
Total	18.4	81.6	100	32.1	67.9	100

Topographic maps (Figures 2 a and c) illustrate the interpolated proportion of different test results across electrodes, highlighting distinct topographic distributions. For EEG test results (Figure 2a), linearity (Gaussian or not) is classified most frequently at central electrodes. In contrast, iEEG shows that Gaussianity and linearity are predominant in the frontal region, while non-Gaussianity and linearity are frequent in the occipital area but less so in the right frontal area (Figure 2c). Though Gaussianity and nonlinearity both EEG expresses highly in the frontal areas, it seems absent in the percetage. EEG

reveals an anterior-to-posterior increase, peaking at occipital electrodes. In contrast, iEEG is mainly central, with asymmetric distribution in the occipital lobes, predominantly on the right.

An alternative perspective is offered by plotting the proportion of test result type over the triangular frequency domain (f_1, f_2) and $f_1 + f_2 \leqslant 50\,\mathrm{hz}$ (corresponding to the bicoherence principal domain) (Figure 2b,d). Note that here, though we deal with statistics for each f_1, f_2) pair, the threshold for deciding tests is the global one for the whole triangular plane, corrected for FDR. Also, by construction, the Gaussianity threshold $c_\alpha^{(G)}$) and the linearity threshold $c_\alpha^{(L)}$ are related as $c_\alpha^{(L)} > c_\alpha^{(G)}$, for individual tests, resulting in a zero proportion of nonlinear but Gaussian results (lower left of Figures 2 b and d). A diagonal ridge of Non-Gaussian Linear test results suggests time domain asymmetries of waveforms for all frequencies. Note, however, the off-diagonal bands of interference coupling for the Alpha frequency harmonics suggest frequency doubling and intermodulation effects. Note the localized bicoherence peak at (10 Hz, 10 Hz) associated with Nonlinearity and Non-Gaussianity. This result indicates evidence of intra-band nonlinear coupling in the alpha rhythm. The iEEG (Figure 2d) shows test proportion on the frequency triangle like those in Figure 2b for the EEG. However, the distribution of the iEEG test proportions seems more smeared on the frequency triangle when compared to scalp EEG data.

It is instructive to view the topographies of the peak frequencies at which the spectrum is maximum, $f_{S_{\max}} = \underset{f}{\operatorname{argmax}}\,(S(f))$, and at which the bicoherence is maximum $f_{b_{\max}} = \underset{f'}{\operatorname{argmax}}\,(b(f', f'))$. The latter is restricted to the bispectral values on the main diagonal of the principal domain. The occipital and parietal areas are in the alpha band, while in the frontal region, it slows down to the theta band. The peak frequency of the bicoherence is higher than the peaks found by the spectrum.

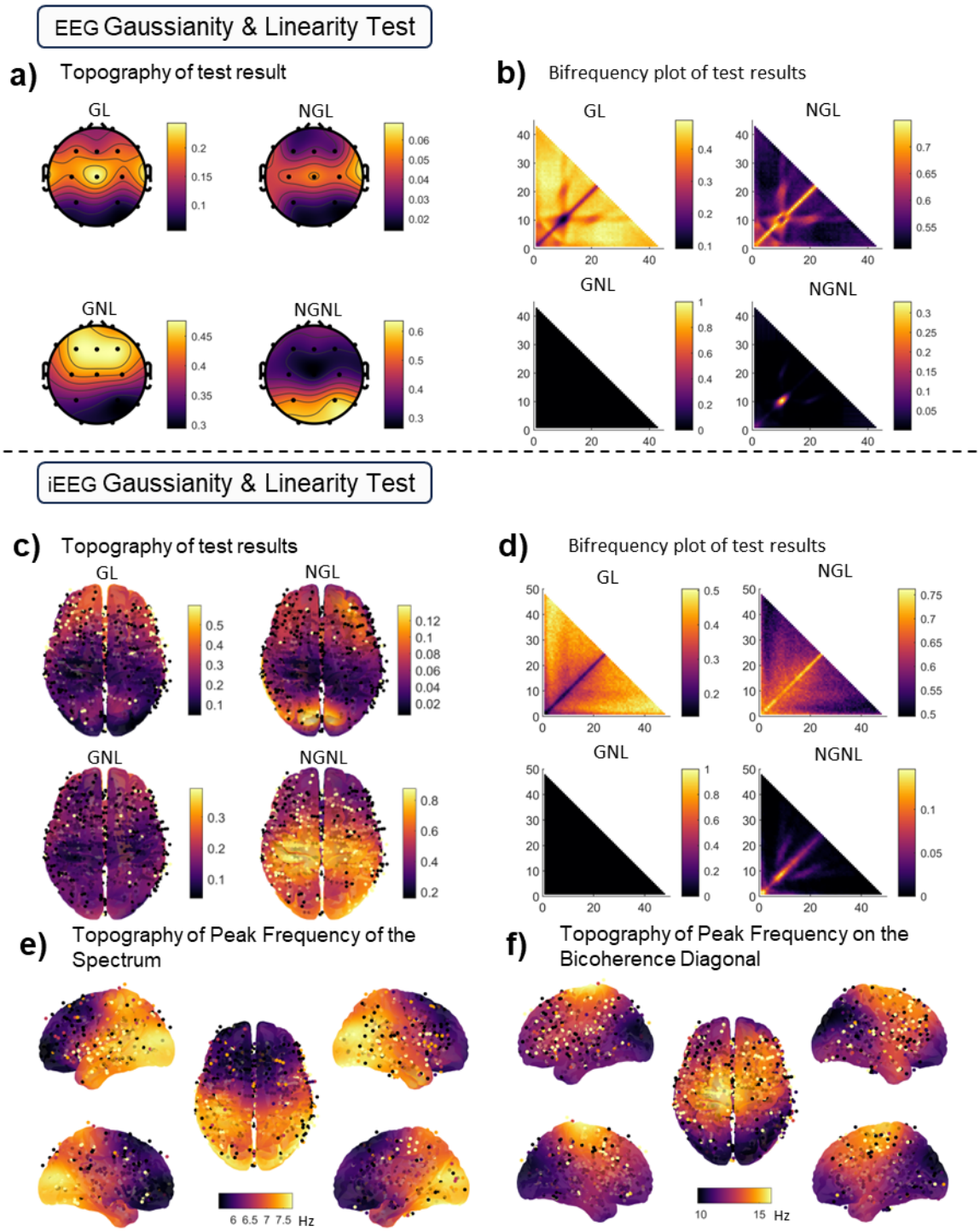

Figure 2. This figure presents the results of Gaussianity and linearity tests applied to iEEG and scalp EEG recordings. *(a) The topography map of the proportion of test classes of EEG data; (b) the proportion of test class of EEG along the bifrequency panel; (c-d) the spatial distribution of the frequency for the maximum spectrum peak and bicoherence peak after remove the Xi trend; (e) the surface plot interpolated by the statistical significance of iEEG channels; (f) the proportion of test class of iEEG along the bifrequency panel.*

2.2 Nonlinear resonances manifest in Rho peaks, while the Xi process remains linear and Gaussian

Besides identifying the non-Gaussianity and nonlinearity of the complete signal, we apply the statistical test to each component separated by the BiSCA model. To avoid the influence of volume conduction here, we work on the iEEG data.

Figure 3a shows the distribution of the Gaussianity test statistics for each component relative to the significance threshold. The $b^{(G)}$ of full signal is located around the threshold, while the statistics for the aperiodical Xi process and periodical Rho process are much lower than the threshold, indicating they are less non-Gaussian than the composite signal. The correlation of non-Gaussianity between the full signal and its components is moderate for the Rho process (Figure 3e) and weaker for the Xi process (Figure 3f).

When the system is nonlinear, the bicoherence of non-Gaussianity cannot be modeled as a pure constant. Therefore, the nonlinearity in figure 3b is more important. The right subplot (Figure 3b) shows the bicoherence statistic for nonlinearity. The $b^{(L)}$ of full signal and the Rho process are much higher than the threshold, indicating significant nonlinearity. In contrast, the statistic for the Xi process is not, suggesting it behaves linearly. This finding is further supported by the correlation analysis in Figures 3c-f. There is a strong, positive correlation between the full signal's nonlinearity and the Rho process's nonlinearity (Figure 3c), whereas the correlation is much weaker for the Xi process (Figure 3d). The BiSCA model successfully separates and parametrizes nonlinear resonance activity (Rho component) from linear background activity (Xi component). The Rho activities, including Alpha rhythms, exhibit significant nonlinear resonance as evidenced by their bicoherence patterns, while the Xi component shows minimal nonlinear resonance contributions.

Figures 3g-l illustrate the spatial distribution of energy and statistical features for each component across the brain. The energy of each electrode has been corrected by solving the Incomplete Observed Linear Mixture Model (IOLMM) model. The energy of the aperiodical Xi process is broadly distributed, with notable concentrations in the occipital lobe, temporal lobe, and left parietal lobe(Figure 3g). The energy of the periodical Rho process shows a more focal distribution, with high energy localized explicitly in the occipital lobe and an anterior-to-posterior decrease toward the prefrontal cortex (Figure 3h). The spatial patterns of the Gaussianity statistic are tiny. Basically, the non-gaussianity of the Xi process has a higher value in the frontal region, and the Rho processes have a higher value in the

occipital and parietal regions. The maps for the nonlinearity statistic reveal a clear distinction. The Xi process exhibits low nonlinearity across the entire brain (Figure 3k), consistent with its linear nature. Conversely, the Rho process shows high nonlinearity in regions exhibiting high energy, particularly in the temporal and parietal lobes (Figure 3l). This colocalization reinforces the conclusion that the periodic Rho component is the principal source of nonlinear dynamics in the observed brain activity. The nonlinearity in the parietal is higher than the occipital because the Mu process's origin is in the parietal lobe, which has more nonlinearity than the Alpha. By the bicoherence, this is the first time the Mu and Alpha have intracranial data, showing that even Alpha's energy is much stronger than the Mu. Still, the bicoherence is entirely different, while we did not observe it in the scalp data.

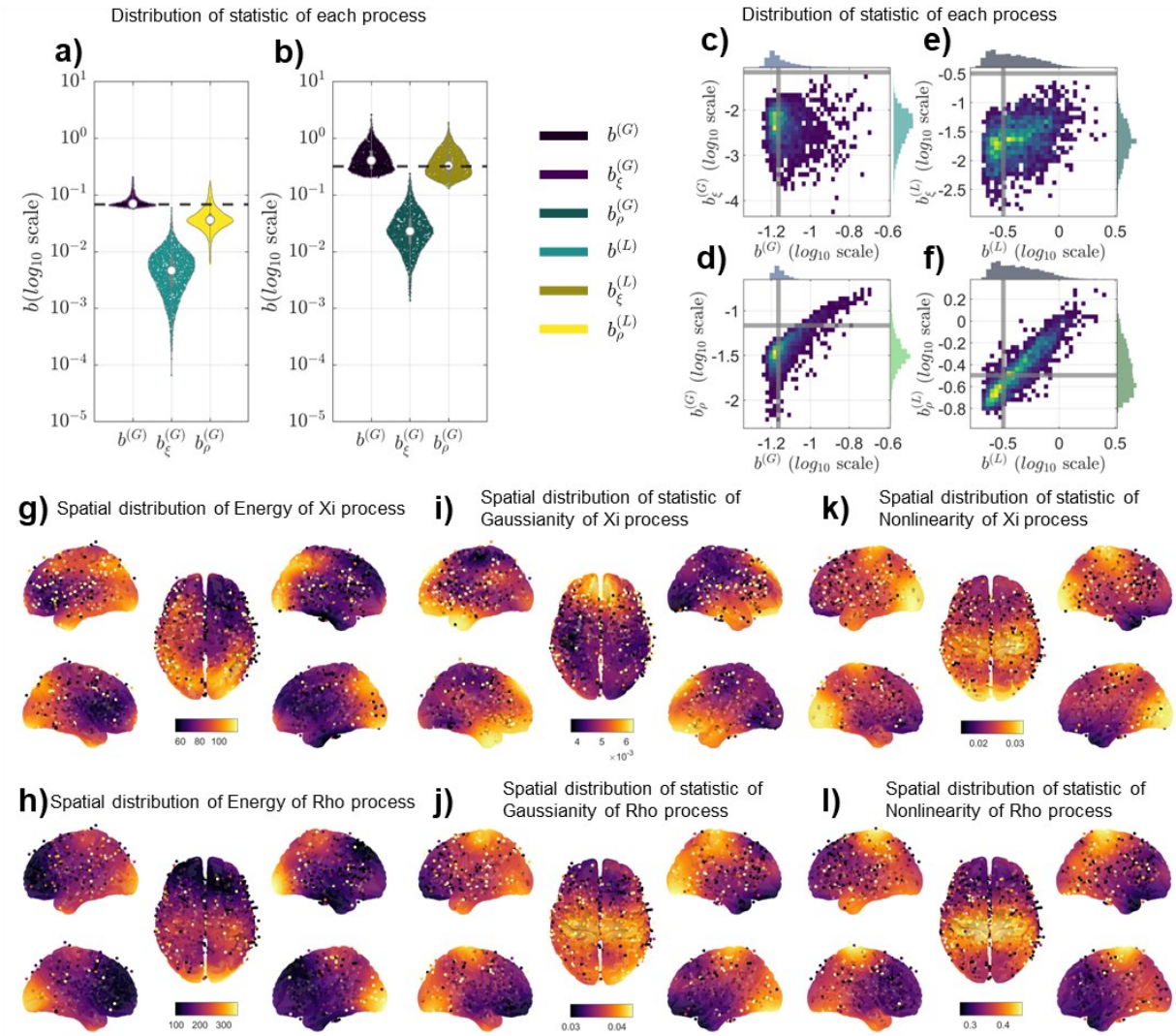

Figure 3: Statistical features of iEEG signals decomposed into Xi trends and periodical Rho components. *(a-b) Violin plots showing the distribution of the (a) Gaussianity statistic $b^{(G)}$ and (b) nonlinearity (bicoherence) statistic $b^{(L)}$ for the full signal, the aperiodical Xi process (ξ), and the periodical Rho process (ρ). The dashed line indicates the threshold for statistical significance. (c-f) Scatter plots showing the relationship between the full signal and its components. Plots (c-d) show the correlation between the Gaussianity statistics of the full signal and the (c) Rho process and the (d) Xi process. Plots (e-f) show the correlation between the linearity statistic of the full signal and the (e) Rho process and the (f) Xi process. (g-l) Topographical maps of the brain showing the spatial distribution of key statistics for the aperiodical Xi and Rho processes. (g-h) Spatial distribution of energy. (i-j) Spatial distribution of the Gaussianity statistic $b^{(G)}$. (k-l) Spatial distribution of the nonlinearity statistic $b^{(L)}$. Red indicates higher values, while blue indicates lower values.*

3. Discussion

This study investigated the non-Gaussian and nonlinear properties of neural signals by decomposing resting-state EEG and iEEG data into two fundamental components: a wideband, aperiodic process (Xi, ξ) and narrowband, resonant oscillations (Rho, ρ). While previous spectral parameterization methods have

successfully characterized the power-spectral features of these components, they are blind to phase relationships and therefore cannot assess their nonlinearity. To address this gap, we introduced Bispectral EEG Component Analysis (BiSCA), a novel likelihood-based model that unifies spectrum and bispectrum analysis to distinguish and characterize the linear and nonlinear properties of neural signal components.

By analyzing a large dataset of 1,771 intracranial EEG (iEEG) and 1,391 scalp EEG channels, we demonstrate that whole-brain signals are a mixture of processes with distinct higher-order statistical properties. Our analysis reveals that the wideband Xi (ξ) component, often considered purely aperiodic, does not contribute to the quadratic nonlinearity measured by bicoherence. In contrast, the resonant Rho (ρ) components, particularly the Alpha and Mu rhythms, exhibit significant and robust nonlinearity, identifying them as the primary source of this phenomenon in resting-state brain activity.

3.1 Differences between the power spectrum and nonlinear distribution

Figure 2e and 2f illustrate a key finding: the spatial distribution of peak power (from the spectrum) is not equivalent to the distribution of peak nonlinearity (from the bicoherence). This dissociation can be attributed to the distinct properties and locations of the Alpha and Mu rhythms (Figure 3h and 3I). The Alpha rhythm, which dominates the power spectrum, is primarily localized to the occipital region. The Mu rhythm, however, is characterized by a more asymmetric waveform and thus stronger quadratic nonlinearity. Although it has lower energy in the resting state, its nonlinear signature is concentrated over the sensorimotor cortex.

This observation is consistent with Frauscher et al., (2018), who reported that there is power peaks coexist in Alpha and Beta band in the parietal lobe, while only peaks in Alpha band appear in the occipital lobe. Our bicoherence analysis, however, advances these findings by pinpointing more specific, functionally distinct sources of nonlinearity. This dissociation between the spatial patterns of power and bicoherence is corroborated by similar EEG source-reconstruction study (Shahbazi Avarvand et al., 2018).

3.2 The difference between source technology and scalp nonlinearity

Figure 2 reveals a counterintuitive result: the percentage of scalp EEG channels showing significant nonlinearity is not lower than that observed in iEEG recordings. This finding can be directly attributed to the effects of volume conduction. While a nonlinear source like the Mu rhythm originates from a

localized cortical area (e.g., the sensorimotor cortex), its electrical signature is not confined to the overlying scalp electrodes. Instead, volume conduction smears this activity across the scalp, causing the nonlinear features to be detected by a wide array of channels, including those far from the source.

In contrast, iEEG, with its high spatial precision, registers this nonlinearity only on the few electrodes placed directly over the active cortical tissue. Therefore, the spatial leakage of a few strong nonlinear sources in EEG leads to a high percentage of channels being flagged as nonlinear, explaining why this proportion is comparable to that seen in iEEG.

3.3 Bicoherence reveals the dissociable roles of Rho and Xi in cortical dynamics

The analytical separation of components in BiSCA is theoretically grounded in two principles. First, for statistically independent processes, the cumulant spectrum (including the bispectrum) is additive (Brillinger, 2001). Second, and more broadly, even for coupled nonlinear systems described by Volterra functional series (Marzocca et al., 2008; Nichols et al., 2009), the bispectrum can be expressed as a sum of additive components. Each component is analytically defined by the system's linear and quadratic transfer functions, allowing for the formal description and identification of nonlinear interactions.

From the biophysical origin of components, followed the assumption of the organization of different components (Pascual-Marqui et al., 2022), a key theoretical principle of BiSCA is that if two processes are additive and independent from different layers of the cortex (Silva et al., 1991; Van Kerkoerle et al., 2014; Mendoza-Halliday et al., 2024) and a recent study provides a neurophysiological basis for this aperiodic trend, demonstrating with biophysical modeling and experimental evidence that it is a genuine signal generated by arrhythmic network activity, rather than merely an artifact of overlaid brain rhythms (Brake et al., 2024).

This framework of a composite signal—mixture of linear and nonlinear components—helps resolve debates on whether macroscopic EEG dynamics are inherently nonlinear and thus require nonlinear models (Nozari et al., 2024; Raffaelli et al., 2024). Our simulations (Figure 2) further confirm that bispectral analysis uniquely distinguishes these true nonlinear interactions from simple non-Gaussianity arising from other sources. This implies that to accurately model such composite signals, advanced statistical approaches are needed, such as likelihood functions designed for higher-order statistics (Pfanzagl, 1969; Rice, 1979; Leonenko et al., 1998; Anh et al., 2004, 2007a, 2007b; Sakhno, 2014, 2020).

3.4 The Linear Nature of the Aperiodic Component: An Empirical Finding, Not a Universal Law

A central finding of our study is that the aperiodic (Xi, ξ) component of the EEG signal—which is widely considered to exhibit a 1/f-like power law—is predominantly linear. At first glance, this observation may appear to challenge established theories where 1/f spectra can arise from nonlinear dynamics such as self-organized criticality. However, our conclusion is not a universal claim about the origin of all 1/f processes, but rather a specific, data-driven insight into large-scale neural dynamics. Our BiSCA framework reveals that the macroscopic EEG signal is a composite of distinct processes. This means the brain's nonlinearity is not absent; it is instead compartmentalized within the resonant (Rho) oscillations. The linearity of the Xi component can thus be understood as an emergent property, likely arising from the superposition of numerous weakly correlated neural sources where nonlinearities are averaged out at the macroscopic scale.

This empirical finding is strongly corroborated by recent theoretical models. For instance, Kramer & Chu, (2024) demonstrated that a general, noise-driven dynamical system, when linearized around a stable equilibrium, naturally generates spectra with 1/f-like characteristics. Their work provides a compelling theoretical foundation for why a macroscopically linear stochastic process can produce the observed aperiodic background without invoking complex nonlinear mechanisms. It is also crucial to consider the specificity of our methodology; the bicoherence is a powerful tool for detecting quadratic nonlinearity, and our results show a definitive lack of such second-order interactions in the Xi component. While we cannot formally exclude other, more complex forms of nonlinearity, our work robustly refines the debate on neural linearity. In summary, within resting-state EEG, the aperiodic background behaves as a linear stochastic process, while significant, measurable nonlinearity is robustly confined to the oscillatory Rho components.

3.5 Geometric Interpretation links Bicoherence and System Dynamics

The geometric interpretation of bicoherence provides critical insights into system dynamics. For an asymmetric system (Figure 4a-f), significant bicoherence between the fundamental frequency (8.7 Hz) and its second harmonic (17.4 Hz) signifies quadratic phase coupling. This interlocking of phases constrains the system's trajectory in phase space to a specific manifold, manifesting as an asymmetric "wicket" waveform and a distorted limit cycle in the phase portrait. Conversely, for a symmetric system (Figure 4g-k), the bicoherence is zero, reflecting the absence of phase coupling. The system's trajectory

is unconstrained, resulting in a uniform limit cycle and a time-domain waveform with only odd-order harmonics. This contrast highlights how bicoherence geometrically quantifies the degree of asymmetry in the system's underlying potential landscape. Furthermore, bicoherence helps distinguish system-based nonlinearity from non-Gaussian noise. In a nonlinear system, the energy landscape imposes state-dependent constraints, suppressing noise-induced perturbations more effectively in regions with strong recovery forces (e.g., steep potential wells). This state-specific "filtering" of non-Gaussian inputs reduces the measured bicoherence compared to a linear system, where such perturbations propagate homogeneously (Figure A.2). This distinction underscores the importance of modeling both system nonlinearity and noise non-Gaussianity when interpreting higher-order spectral features.

The geometric interpretation of bicoherence reveals critical insights into the nonlinear dynamics of the system, particularly in how phase coupling shapes its oscillatory behavior. In the asymmetric system, the bicoherence plot (Figure 4f) shows significant phase coupling between the fundamental frequency at 8.7 Hz and its second harmonic at 17.4 Hz, indicating quadratic nonlinear interactions that constrain the system's trajectory in phase space to a manifold reflecting these phase-locked oscillations. This interlocking of phases manifests as the asymmetric morphology in the time-domain waveform of the Wicket (Figure 4a), with the directional bias corresponding to imbalanced phase relationships. The reconstructed phase portrait (Figure 4c) supports this, as these nonlinear constraints shape the stable limit cycle's trajectory. Conversely, in the symmetric system, the bicoherence is zero everywhere (Figure 4k), aligning with the regular, balanced oscillations in the time domain (Figure 4g) and the presence of only odd-order harmonics (Figure 4j). Here, the absence of phase coupling results in an unconstrained trajectory in phase space, producing a more uniform limit cycle (Figure 4h). This contrast highlights how bicoherence geometrically quantifies the degree of nonlinearity and asymmetry in the system's dynamics, linking spectral domain insights to the time-domain evolution and the underlying potential landscape (Figures 4d and 4i). These findings underscore the utility of bicoherence in analyzing stability and morphology in nonlinear oscillatory systems, offering a framework to explore the interplay between structure and dynamics.

On the other hand, non-Gaussian innovation introduces an asymmetric distortion to the phase portrait, as seen in linear systems where deviations manifest uniformly due to the absence of state-dependent damping or recovery forces. However, in nonlinear systems, the heterogeneity of the energy landscape imposes a state-dependent constraint on these deviations. For instance, regions of strong recovery strength (e.g., steep potential wells) suppress asymmetric noise-induced perturbations more effectively

than states in flatter landscape regions. This leads to a non-uniform distortion that linear assumptions cannot capture. Consequently, bicoherence shows reduced magnitudes in nonlinear systems Figure A 2 compared to linear counterparts, where deviations are constant across frequencies. The nonlinear case's lower bicoherence reflects the system's capacity to "filter" non-Gaussian perturbations in a state-specific manner, contrasting with the homogeneous propagation of asymmetry in linear frameworks. This distinction underscores the importance of modeling both noise non-Gaussianity and system nonlinearity when interpreting higher-order spectral features.

3.6 Methodological Breakthrough: BiSCA Model

The BiSCA framework addresses two fundamental limitations of existing EEG models: Joint spectrum-bispectrum parametrization captures linear energy decay (Xi) and nonlinear harmonics (Rho), extending the work of parameterizing the EEG frequency components to a 3rd-order spectrum model, allowing to capture the phase information of components. Likelihood-based optimization enables statistical validation of component properties, providing criteria for model comparison.

3.7 Limitations and Future Directions

3.7.1 Determining the Source of Gaussianity of a nonlinear system is a challenge

In nonlinear systems, assessing non-Gaussianity is challenging because non-Gaussian behavior can arise from multiple sources. The system's inherent nonlinearity and non-Gaussian innovations (e.g., stochastic inputs or noise) can contribute to deviations from Gaussianity. Nonlinear transformations of Gaussian inputs can produce non-Gaussian outputs, while non-Gaussian innovations, such as heavy-tailed or skewed noise distributions, further complicate the system's statistical properties.

3.7.2 Multivariate parametric modeling to reveal the higher-order interactions

Since the brain is a coupled distributed system, as discussed by Takens' embedding theory(Takens, 1985; Stark et al., 1997), single channel observations may reconstruct the dynamic property of the whole neural system. However, to be more accurate, the parameterization of spectrum and bispectrum still need to be extended to multivariate to mine the cross-frequency coupling between regions, as the previous studies on coherency (Valdés et al., 1992) and cross-bicoherence (Jirsa & Müller, 2013; Shahbazi Avarvand et al., 2018), which will help to study the nonlinear interaction between the regions in the future.

3.7.3 Extend the higher-order spectral analysis to nonstationary EEG/iEEG

This paper analyzes the system's quadratic nonlinearity (bispectrum/bicoherence) from the stationary perspective. Other nonlinear properties include multistability from a series of works in the time domain (Freyer et al., 2009, 2011, 2012) of the EEG data, which show that a linear system with a single global attractor is an insufficient model. The bicoherence approach provides a complementary perspective. As an effective tool for analysis within local, quasi-stationary windows, it can specifically identify and isolate stationary quadratic interactions that may persist across transitions between attractor states (Wang et al., 2025). This duality between stationary and dynamic perspectives underscores the complex nature of neural signals, which simultaneously exhibit both stable nonlinear features and transient dynamical shifts.

3.8 Conclusion

By rigorously distinguishing linear (Xi) and nonlinear resonant (Rho) EEG components through their unique bispectral fingerprints, this study establishes nonlinear resonance as a core mechanism in resting-state brain dynamics. The BiSCA model provides the first systematic framework to detect and quantify this resonance, challenging the sufficiency of purely linear spectral methods. These results have important implications for developing more accurate neural models and for analyzing EEG data in both research and clinical settings. Future work should explore the functional significance of nonlinearity in the Rho component and investigate how these properties are modulated across different cognitive states and neurological conditions.

4. Materials and Methods

4.1 Materials

EEG Dataset: Resting-state EEG data from 960 healthy participants were analyzed using the subset of globally diverse HarMNqEEG dataset (Li et al., 2022), excluding Medicid-4-Cuba-2003 and other samples recorded for less than 1 minute, comprising 14 studies across 9 countries. Data included 18 channels (excluding Pz) from the 10-20 system after average referencing. Participants were selected from normative or control groups, excluding those with neurological/psychiatric conditions. Channels were retained if artifact-free, with no interictal discharges or slow-wave anomalies, and recordings consisted of eyes-closed resting-state data. Preprocessing involved converting signals to an average reference,

segmenting data into 2.56s epochs (0.39 Hz resolution), and subsampling to have 157 segments per subject to align with iEEG data consistency requirements.

iEEG Dataset: Resting-state Intracranial EEG (iEEG) data from 106 patients with refractory focal epilepsy (1,772 electrodes) were analyzed to minimize volume conduction and muscular artifacts. Data from the Montreal Neurological Institute included sEEG/ECoG recordings from non-lesional, non-seizure onset zones, free of interictal discharges, slow-wave anomalies, or post-seizure/stimulation effects. Preprocessing involved bandpass filtering (0.5–80 Hz), downsampling to 200 Hz, and removing zero-valued artifacts. The study focused on 60-second eyes-closed resting-state wakefulness recordings, ensuring data integrity for linearity and Gaussianity analysis while reducing dimensionality and computational load.

4.2 Method

4.2.1 Multitaper Estimator for the Spectrum

The frequency domain representation captures the steady-state statistics of the signal. Besides the spectrum for linear Gaussian, the higher-order spectrum for linearity and Gaussianity is introduced.

Each segment of the signal was subjected to a Discrete Fourier transform $X(f) = \frac{1}{N_t}\sum_{t=0}^{N_t-1} x[t]e^{-j2\pi ft}$. To balance the frequency resolution and computational resources, in our study, the window size is 300 time points (1.5 seconds), and segments are 75% overlapping. From this, we calculated the empirical power spectrum $\widehat{S}(f) = \mathrm{E}[X(f)X^*(f)]$ using the multitaper method $x_k(t) = x(t)v_k(t)$ (Thomson, 1982; He & Thomson, 2010) to reduce the spectral frequency leakage bias and increase the smoothness of the spectrum with its nonparametric smooth property in the frequency domain. The tapers v_k are the orthonormal windows instead of Discrete Prolate Spheroidal (Slepian) Sequences (DPSS), we used the Sine taper (Riedel & Sidorenko, 1995) to avoid the bias of amplitude. Therefore,

$$X_{k,e}(f) = \frac{1}{N_t}\sum_{t=0}^{N_t-1} x_{k,e}(t)e^{-j2\pi ft} \tag{1}$$

$$\widehat{S}_k(f) = X_{k,e}(f)X^*_{k,e}(f) \tag{2}$$

$$\widehat{S}(f) = \frac{1}{U_2}\sum_{k=0}^{K-1} \widehat{S}_k(f) \tag{3}$$

where $U_2 = K/N_t$. In this paper, we use $NW = 1.5$, i.e. $K = 2NW - 1 = 4$ for the recordings. NW is a critical parameter that controls the trade-off between frequency resolution (how finely you can distinguish between nearby frequencies) and variance (how noisy the spectral estimate is).

4.2.2 Multitaper Estimator for the Bispectrum

As the power spectrum is the 2nd-order cumulant spectrum, the nth-order cumulant spectrum was be defined (Brillinger & Rosenblatt, 1967a, 1967b). The bispectrum is a function of bifrequency f_1 and f_2

$$B(f_1, f_2) = \mathrm{E}[X(f_1)X(f_2)X^*(f_1 + f_2)] \tag{4}$$

is the 3rd-order cumulant spectrum. It is a third-order spectral statistic that extends the power spectrum to capture quadratic nonlinear interactions between different frequency components. It measures the degree of quadratic nonlinear interaction by assessing the consistency of phase relationships between frequency pairs f_1 and f_2 and their sum $f_1 + f_2$, constrained by the stationarity condition $f_1 + f_2 = f_3$. This condition arises from the process's stationarity and translation invariance, leading to energy conservation in nonlinear interactions.

There are several versions to normalize the bispectrum (Shahbazi et al., 2014), here we use the version that keeps the value of the normalized skewness of the process, which benefits the statistical test in the next section. So, this paper uses the bicoherence

$$b(f_1, f_2) = \frac{B(f_1, f_2)}{\sqrt{S(f_1)S(f_2)S(f_1 + f_2)}} \tag{5}$$

For example, in the bicoherence plot (e.g., Figure 4f), significant phase coupling is visualized as high values along the frequency grid, indicating that the phases of these frequencies are interlocked. For the symmetric system (Figure 4k), the bicoherence is zero everywhere, reflecting the absence of phase coupling due to the presence of only odd-order harmonics, as seen in the spectrum (Figure 4j). This geometric representation allows bicoherence to bridge spectral domain analysis with the system's nonlinear dynamics, complementing the multitaper estimator's ability to detect and quantify such interactions in oscillatory systems like the Wicket wave (Figure 4a).

The Multitaper estimator for the bispectrum and bicoherence (Thomson, 1989; Birkelund et al., 2001)

$$\hat{B}_{k_1k_2k_3}(f_1,f_2) = X_{k_1,e}(f_1)X_{k_2,e}(f_2)X^*_{k_3,e}(f_1+f_2) \tag{6}$$

$$\hat{B}(f_1,f_2) = \frac{1}{U_3}\sum_{k_1k_2k_3=0}^{K-1} P_{k_1k_2k_3}\hat{B}_{k_1k_2k_3}(f_1,f_2) \tag{7}$$

To preserve the correct scale, the 'bienergy' $P_{k_1k_2k_3} = \sum_{t=0}^{N_t-1} v_{k_1}(t)v_{k_2}(t)v_{k_3}(t)$ and $U_3 = \frac{1}{N_t}\sum_{k_1,k_2,k_3}^{K} P^2_{k_1k_2k_3}$.

The bicoherence measures the asymmetric degree of phase coupling between frequencies.

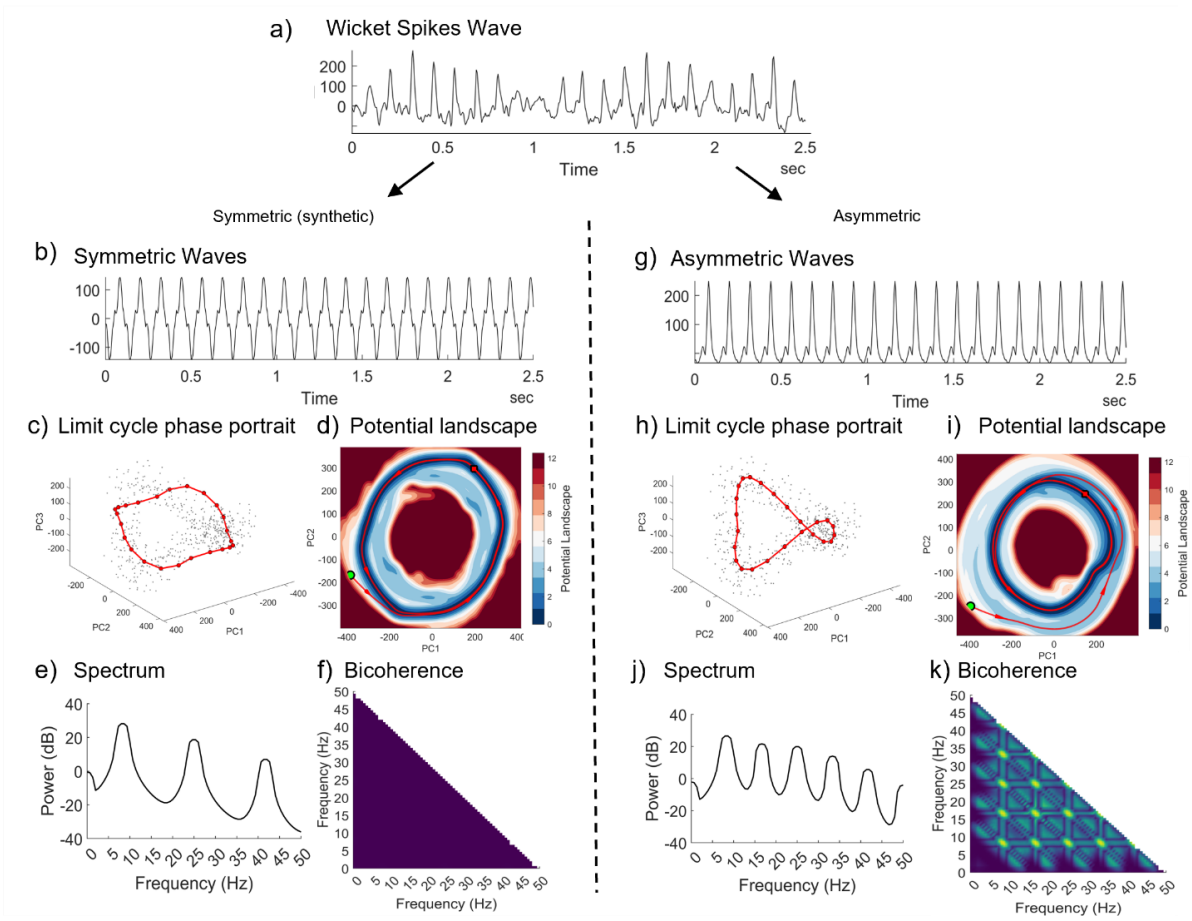

Figure 4 Geometric interpretation of bicoherence. *a) Wicket wave segmented from the iEEG data; b) limit cycle wave form of the coreset extracted by the NNAR model from the Wicket wave, detailed steps are in the appendix. c) 3D visualization of this limit cycle phase portrait (red) and coreset (gray); d) the potential landscape of the Wicket estimates with the density function of multiple trials of 2D noise simulation, red trajectory are noise-free simulation; e) spectrum of the limit cycle; f) bicoherence of this limit cycle.*

4.2.3 Test for Gaussianity and linearity through Higher-Order Spectrum

A key distinction between linear and nonlinear systems lies in their treatment of frequency components. A linear system processes each frequency component of an input signal independently. In contrast, even

a weakly nonlinear system introduces interactions between frequencies, fundamentally transforming the signal's state-space. This phenomenon, which Jirsa & Müller (2013) attribute to a "symmetry breaking" in the system's dynamics, results in the generation of new frequencies through harmonic and intermodulation distortion. Bicoherence $b(f_1, f_2)$ is a higher-order spectral measure specifically designed to detect and quantify these interactions. It reveals quadratic nonlinearity by measuring quadratic phase coupling—a consistent phase relationship between two frequencies (f_1 and f_2) and their sum frequency $f_1 + f_2$. A significant bicoherence value indicates an efficient, phase-dependent transfer of energy from the fundamental frequencies to a new, combined frequency. This reflects underlying modulatory processes and serves as direct evidence that the system deviates from linearity.

On the other hand, the bicoherence for non-Gaussian but linear processes can also be non-zero. To distinguish a linear non-Gaussian process and a nonlinear process, we can use the property of n-th order coherency function for the linear system, which can be expressed as (C. Nikias & Petropulu, 1993)

$$C_n^y(\omega_1, ..., \omega_{n-1}) = \frac{\gamma_n^x}{(\gamma_2^x)^{n/2}} \frac{H(\omega_1)H(\omega_2)\cdots H(\omega_{n-1}) \cdot H^*(\omega_1 + \cdots + \omega_{n-1})}{|H(\omega_1)|\,|H(\omega_2)|\cdots|H(\omega_{n-1})| \cdot |H^*(\omega_1 + \cdots + \omega_{n-1})|} \tag{8}$$

The $H(w)$ is the first order frequency transfer function for the linear time-invariant (LTI) system. The γ_n^x is nth order cumulant. The magnitude of the nth-order coherency function is a constant value for all the frequencies:

$$|C_n^y(\omega_1, ..., \omega_{n-1})| = \frac{\gamma_n^x}{(\gamma_2^x)^{n/2}}$$

The test for Gaussianity and Linearity has been discussed in many literature (Hinich, 1982; C. Nikias & Petropulu, 1993; Berg et al., 2010): the test of Gaussianity can be formed by testing if the normalized bispectrum, i.e., bicoherence $C(\omega_1, \omega_2)$ has zero constant deviation; the linearity test can be formed by testing if the normalized bispectrum is constant. In other words, if the value of nth-order coherence depends on frequency $f_1, f_2, \cdots, f_{n-1}$, then the process is nonlinear. Specifically, the linear Gaussian process is constantly equal to 0, i.e. $|C_n^y(\omega_1, ..., \omega_{n-1})| = 0$ for all $n > 2$.

4.2.3.1 Distribution

The bispectrum asymptotically follows the complex Gaussian distribution (Brillinger & Rosenblatt, 1967a)

$$\mathrm{E}\left[\hat{B}(f_1, f_2)\right] = B(f_1, f_2) \tag{9}$$
$$\mathrm{Var}\left[\hat{B}(f_1, f_2)\right] = S(f_1)S(f_2)S(f_1 + f_2)$$

4.2.3.2 Statistical test for Gaussianity and linearity

Therefore, we can apply statistical tests for Gaussianity and linearity based on bicoherence. The test proposed by (Hinich, 1982) addresses a multimodal distribution problem, where deviations from Gaussianity and linearity manifest as distinct modes in the bicoherence distribution. However, this approach, which sums squared bicoherence values across frequency pairs and compares the result to a chi-squared distribution, is overly sensitive to extreme values caused by localized nonlinear interactions. This sensitivity can lead to false positives when the goal is to detect widespread non-Gaussianity. Similarly, traditional interquartile range (IQR) tests for linearity are insensitive to narrow-band quadratic phase coupling, as they focus on the central dispersion and miss sparse extreme values indicative of isolated nonlinear peaks. We propose two robust tests to address these limitations: a median-based test to assess central tendency for Gaussianity and diffuse nonlinearity and a maximum-based test to detect strong, localized nonlinear interactions.

The first test focuses on the median of the squared bicoherence values, offering a robust measure of typical phase coupling that is less affected by outliers. The test statistic is defined as:

$$t^{(G)} = 2N_s \cdot \underset{f_1, f_2}{\mathrm{median}}\{|b(f_1, f_2)|^2\}$$

where N_s is the number of segments, and the median is computed over all unique frequency pairs (f_1, f_2). Under the null hypothesis of Gaussianity and linearity, this statistic follows an asymptotic normal distribution (see the appendix for details). The test evaluates:

$$P\{t^{(G)} > c_\alpha^{(G)}\} \approx \alpha \tag{10}$$

where $c_{\alpha_{\mathrm{stat}}}$ is the critical value from the asymptotic normal distribution at the significance level α_{stat}. This test excels at detecting diffuse non-Gaussianity or widespread weak nonlinearity, providing a stable alternative to the original Hinich test.

To identify strong, localized nonlinear interactions, we introduce a test based on the maximum squared bicoherence value, adjusted for baseline non-Gaussianity. The test statistic is:

$$t^{(L)} = 2N_s \cdot \max_{f_1, f_2}\{|b(f_1, f_2)|^2\}$$

We estimate a non-centrality parameter λ_0 using the median of the scaled bicoherence values to account for non-Gaussianity. The distribution of $T_{\max}$ is modeled using extreme value theory, specifically a Gumbel distribution, with parameters derived from λ_0 and the number of frequency pairs (see appendix for details). The test evaluates:

$$P\{t^{(L)} > c_\alpha^{(L)}\} \approx \alpha \tag{11}$$

where $c_{\alpha_{\text{stat}}}$ is the critical value from the Gumbel distribution at the significance level α_{stat}. This test is designed to pinpoint significant localized nonlinearity beyond the baseline level.

4.2.4 BiSpectral EEG Component Analysis (BiSCA)

4.2.4.1 Whole model

After obtaining the empirical and higher-order spectra, this paper proposed a BiSCA model specifically designed to detect nonlinear resonance by jointly parametrizing the spectrum and bispectrum. This combined model approach is essential for identifying nonlinear resonance phenomena that cannot be detected by traditional spectral analysis alone. Here, the Xi trend and Rho peaks (including Alpha and all other oscillatory peaks) are modeled with two types of independent processes, allowing them to be additive on the natural scale. Additionally, the analysis includes both the spectrum and the bispectrum to understand the components comprehensively.

$$S(f;\theta_{2,\xi},\theta_{2,\rho}) = S_\xi(f;\theta_{2,\xi}) + S_\alpha(f;\theta_{2,\rho}) \tag{12}$$

$$B(f_1, f_2;\theta_3) = B_\xi(f_1, f_2;\theta_{3,\xi}) + B_\rho(f_1, f_2;\theta_{3,\rho}) \tag{13}$$

where different θ are the parameters for different components in each order.

4.2.4.2 Model for Spectrum

In this paper, we put all peaks in the group of Alpha for several reasons. 1) To be consistent with the conventional XiAlpha model, we model the trend as the Xi process and the oscillatory rhythms as the Alpha process. 2) The models of oscillation peaks have similar structures. 3) We focus on univariate

analysis, which views the neural masses as a single integrated oscillator. For the spectra, each component consists of a sum of squares of kernel functions. Since here we use the transfer function to connect different orders of spectra, the sum of the squares of the frequency transfer function of each component approximates the modeled theoretical power spectra here

$$S_{\xi}(f;\sigma_{\xi},\nu_{\xi},d_{\xi}) = h_{S,\xi}t(f;0,\sigma_{\xi},\nu_{\xi},d_{\xi})^{2} \tag{14}$$
$$S_{\rho}(f;\mu_{\rho},\sigma_{\rho},\nu_{\rho},d_{\rho}) = \sum_{k=1}^{K} h_{S,\rho,k}t(f;\mu_{\rho},\sigma_{\rho},\nu_{\rho},d_{\rho})^{2}$$

The kernel function $t(\cdot)$ models the oscillatory rhythm peaks in the spectrum domain. The h is the scale parameter for each peak, and the peak number K represents the number of harmonics to be modeled. We offered two strategies for determining the center frequency of peaks: (1) the $\{\mu_{\rho,k}\}$ is $\left\{\cdots,\frac{1}{3}\mu_{\alpha},\frac{1}{2}\mu_{\alpha},\mu_{\alpha},2\mu_{\alpha},3\mu_{\alpha},\cdots\right\}$, in practice, the order k is chosen with the Akaike information criteria. This circumstance models the alpha rhythm with the simplest condition that the resting state EEG is the output of the system excited with Gaussian white innovation, and the 1st-order transfer function has a single tone at Alpha; the rest of the peaks in other bands are the harmonics of the fundamental oscillation peak. (2) fit each of the $\{\mu_{\alpha,k}\}$ through the spectra and then adjust with the joint fitting with the bispectrum. Option (1) offers frequency peak organization following the conventional broadband analysis; option (2) will fit the components better but is more complicated. This paper demonstrates the result with option (2), which is more general and can use the parameter for bicoherence to interpolate the phase relationship between the peaks. The goodness of both option fit is shown in the appendix.

The student t kernel function has been used in previous studies of spectrum fitting (Pascual-marqui et al., 1988; Newville et al., 2014; Haley & Anitescu, 2017). Here, we modified the student t function to model the amplitude of the 1st-order frequency transfer function, which also extends the adjustable heavy-tail version of the Lorentzian (Cauchy-Lorentz distribution function).

$$t(f,\mu,\sigma,\nu,d) = \frac{1}{\left[1+\left(\frac{f-\mu}{\sigma}\right)^{d}\right]^{\nu}} \tag{15}$$

The parameter σ controls the width of the kernel function. The parameter d controls the flat top of the kernel since the Multitaper method is smooth in the frequency domain and distorts the shape function; in practice, the value is larger than 2. The parameter ν controls the kurtosis or the heavy tail of the peak. Special case: $d=2$ it turns to the student t function; $\upsilon=1$, $d=2$ it turns to the Lorentzian kernel.

4.2.4.3 Model for bispectrum

To simplify the modeling process, we did not directly use the theoretical composition form of transfer function kernels to each order of the spectrum (Marzocca et al., 2008; Nichols et al., 2009; Billings, 2013; Peng et al., 2013; Jing & Lang, 2015). Instead, we focus on capturing the primary relationships of position and order by parameterizing the theoretical bispectrum $M_3(f_1,f_2)$ as follows:

$$\begin{aligned}
\mathrm{Re}[M_3(f_1,f_2)] &= \mathrm{Re}(h_{B,\xi})t_2(f_1,f_2;\mu_\xi,\mu_\xi,\sigma_\xi,\nu_\xi,d_\xi) && \text{‘}\xi\text{’} \\
&\quad + \sum_{m=1}^{K}\sum_{n=1}^{m}\mathrm{Re}(h_{B,\rho,m,n})t_2(f_1,f_2;\mu_{\rho,m},\mu_{\rho,n},\sigma_\rho,\nu_\rho,d_\rho) && \text{‘}\rho\text{’} \\
\mathrm{Im}[M_3(f_1,f_2)] &= \mathrm{Im}(h_{B,\xi})t_2(f_1,f_2;\mu_\xi,\mu_\xi,\sigma_\xi,\nu_\xi,d_\xi) \\
&\quad + \sum_{m=1}^{K}\sum_{n=1}^{m}\mathrm{Im}(h_{B,\rho,m,n})t_2(f_1,f_2;\mu_{\rho,m},\mu_{\rho,n},\sigma_\rho,\nu_\rho,d_\rho)
\end{aligned} \tag{16}$$

This formula captures the essential features of the bispectral peaks without resorting to complex transfer function compositions. The BiSCA models the real and imaginary parts of the bispectrum separately since the phase information of the bispectrum is necessary for discrimination of systems (C. L. Nikias & Mendel, 1993). The kernel function for the bispectrum is

$$t_2(f_1,f_2;\mu_1,\mu_2,\sigma,\nu,d) = \frac{1}{t(f_1;\mu_1,\sigma,\nu,d)t(f_2;\mu_2,\sigma,\nu,d)t(f_1+f_2;\mu_1+\mu_2,\sigma,\nu,d)}$$

4.2.4.4 Likelihood

The likelihood of the model follows the asymptotically Gaussian distribution of the log-scale spectrum (Bevan et al., 1979) and natural scale bispectrum(Brillinger, 1985).

To ensure that the Xi process exhibits a wide spectrum, we add a likelihood term for the Xi process to encourage fits that adhere to the overall trend. The joint likelihood for the full model is:

$$
\begin{aligned}
L\left(\theta_2,\theta_3|\hat{S},\hat{B}\right) &= L\left(\theta_2|\tilde{S}\right) + L\left(\theta_3|\tilde{B}\right) \\
&= -\frac{1}{N_S}\sum_f \left(\frac{\log\left(\hat{S}(f)\right) - \log\left(\tilde{S}(f;\theta_2)\right)}{\widehat{Var}\left[\log\left(\hat{S}(f)\right)\right]}\right)^2 \\
&\quad - \frac{1}{N_B}\sum_{f_1}\sum_{f_2} \frac{\left|\hat{B}(f_1,f_2) - \tilde{B}(f_1,f_2;\theta_3)\right|^2}{\tilde{S}(f_1;\theta_2)\tilde{S}(f_2;\theta_2)\tilde{S}(f_1+f_2;\theta_2)}
\end{aligned}
$$

where the $\hat{S}(f)$ and $\hat{B}(f_1,f_2)$ is the Multitaper power spectrum and bispectrum estimate by formula (3) and (7), $\tilde{S}(f;\theta_2)$ and $\tilde{B}(f_1,f_2;\theta_3)$ is the modeled theoretical power spectrum and bispectrum.

This likelihood-based method makes it advantageous to use statistical methods to do the model comparison.

4.2.4.5 Fit with the Levenberg-Marquardt method

We estimate the model parameters using the Levenberg-Marquardt (LM) optimization algorithm. The LM method is a standard technique for solving nonlinear least squares problems, effectively balancing the Gauss-Newton algorithm and gradient descent. It is particularly suitable when the objective function is the sum of squares of loss functions, as in our joint likelihood estimation, which is also a heteroscedastic curve/surface fitting problem. Employing the LM method, we iteratively update the parameter estimates to minimize the discrepancy between the empirical and theoretical spectrum and bispectrum, ensuring convergence to an optimal solution. The LM algorithm is not a global optimization method. Therefore, we fit the spectra parameters first and then share the parameters with the bispectrum as a warmup for the joint fit.

4.2.4.6 Bicoherence for each component

We can then obtain the bicoherence for each component

$$
\tilde{b}_\xi(f_1,f_2) = \frac{\tilde{B}_\xi(f_1,f_2)}{\sqrt{S(f_1)S(f_2)S(f_1+f_2)}}
$$

$$
\tilde{b}_\rho(f_1,f_2) = \frac{\tilde{B}_\rho(f_1,f_2)}{\sqrt{S(f_1)S(f_2)S(f_1+f_2)}}
$$

To avoid instability during fitting, we use full variance to normalize.

We use full variance to normalize the component bicoherence to avoid instability and ensure the additive way to model the bicoherence.

4.2.4.7 Test for components

Then we recall the test (10) and (11) for testing the non-Gaussianity and linearity of each component.

5. Data availability

The scalp EEG and intracranial EEG (iEEG) data analyzed in this study were obtained from the work of Li et al., (2022) and Frauscher et al. (2018), respectively.

6. Code availability

The analysis code used in this study will be made publicly available in a GitHub repository upon formal publication of this article, and the link will be provided.

7. References

Anh, V. V., Leonenko, N. N., & Sakhno, L. M. (2004). On a class of minimum contrast estimators for fractional stochastic processes and fields. *Journal of Statistical Planning and Inference*, *123*(1), 161–185. https://doi.org/10.1016/S0378-3758(03)00136-8

Anh, V. V., Leonenko, N. N., & Sakhno, L. M. (2007a). Minimum contrast estimation of random processes based on information of second and third orders. *Journal of Statistical Planning and Inference*, *137*(4), 1302–1331. https://doi.org/10.1016/j.jspi.2006.03.001

Anh, V. V., Leonenko, N. N., & Sakhno, L. M. (2007b). Statistical inference using higher-order information. *Journal of Multivariate Analysis*, *98*(4), 706–742. https://doi.org/10.1016/j.jmva.2006.09.009

Barry, R. J., & Blasio, F. M. D. (2021). Characterizing pink and white noise in the human electroencephalogram. *Journal of Neural Engineering*, *18*(3), 034001. https://doi.org/10.1088/1741-2552/abe399

Bédard, C., Kröger, H., & Destexhe, A. (2006). Does the $1/f$ Frequency Scaling of Brain Signals Reflect Self-Organized Critical States? *Physical Review Letters*, *97*(11), 118102. https://doi.org/10.1103/PhysRevLett.97.118102

Berg, A., Paparoditis, E., & Politis, D. N. (2010). A bootstrap test for time series linearity. *Journal of Statistical Planning and Inference*, *140*(12), 3841–3857. https://doi.org/10.1016/j.jspi.2010.04.047

Bevan S., Kullberg R., & Rice J. (1979). An Analysis of Cell Membrane Noise. *The Annals of Statistics*, *7*(2), 237–257. https://doi.org/10.1214/aos/1176344609

Billings, S. A. (2013). *Nonlinear System Identification: NARMAX Methods in the Time, Frequency, and Spatio-Temporal Domains* (1st ed.). Wiley. http://gen.lib.rus.ec/book/index.php?md5=66b2821a252e489f0230a0ba4cb511aa

Birkelund, Y., Hanssen, A., & Powers, E. J. (2001). Multitaper estimation of bicoherence. *2001 IEEE International Conference on Acoustics, Speech, and Signal Processing. Proceedings (Cat. No.01CH37221)*, *5*, 3085–3088 vol.5. https://doi.org/10.1109/ICASSP.2001.940310

Brake, N., Duc, F., Rokos, A., Arseneau, F., Shahiri, S., Khadra, A., & Plourde, G. (2024). A neurophysiological basis for aperiodic EEG and the background spectral trend. *Nature Communications*, *15*(1), 1514. https://doi.org/10.1038/s41467-024-45922-8

Breakspear, M. (2017). Dynamic models of large-scale brain activity. *Nature Neuroscience*, *20*(3), 340–352. https://doi.org/10.1038/nn.4497

Brillinger, D. R. (1985). FOURIER INFERENCE: SOME METHODS FOR THE ANALYSIS OF ARRAY AND NONGAUSSIAN SERIES DATA. *Journal of the American Water Resources Association*, *21*(5), 743–756. https://doi.org/10.1111/j.1752-1688.1985.tb00169.x

Brillinger, D. R. (2001). *Time Series: Data Analysis and Theory*. SIAM: Society for Industrial and Applied Mathematics. http://gen.lib.rus.ec/book/index.php?md5=183bc94159ab7babf5361702f7d9262d

Brillinger, D. R., & Rosenblatt, M. (1967a). ASYMPTOTIC THEORY OF ESTIMATES OF kTH-ORDER SPECTRA*. *Proceedings of the National Academy of Sciences*, *57*(2), 206–210. https://doi.org/10.1073/pnas.57.2.206

Brillinger, D. R., & Rosenblatt, M. (1967b). *Computation and interpretation of k-th order spectra*. https://www.stat.berkeley.edu/~brill/Papers/1967Computation.pdf

Connor, C. W. (2022). Signal, not noise: Aperiodic dynamics in the electroencephalogram under anesthesia. *Anesthesia and Analgesia*, 10.1213/ANE.7577. https://doi.org/10.1213/ANE.0000000000007577

Donoghue, T., Haller, M., Peterson, E. J., Varma, P., Sebastian, P., Gao, R., Noto, T., Lara, A. H., Wallis, J. D., Knight, R. T., Shestyuk, A., & Voytek, B. (2020). Parameterizing neural power spectra into periodic and aperiodic components. *Nature Neuroscience*, *23*(12), Article 12. https://doi.org/10.1038/s41593-020-00744-x

Dragovic, S. Z., Ostertag, J., Baumann, N., García, P. S., Kratzer, S., Schneider, G., Schwerin, S., Sleigh, J., & Kreuzer, M. (2022). Spectral Differences of Anesthetic Agents: Addressing Fundamental Problems With New Methods. *Anesthesia and Analgesia*, 10.1213/ANE.7530. https://doi.org/10.1213/ANE.0000000000007530

Evertz, R., Hicks, D. G., & Liley, D. T. J. (2022). Alpha blocking and 1/fβ spectral scaling in resting EEG can be accounted for by a sum of damped alpha band oscillatory processes. *PLOS Computational Biology*, *18*(4), e1010012. https://doi.org/10.1371/journal.pcbi.1010012

Frauscher, B., von Ellenrieder, N., Zelmann, R., Doležalová, I., Minotti, L., Olivier, A., Hall, J., Hoffmann, D., Nguyen, D. K., Kahane, P., Dubeau, F., & Gotman, J. (2018). Atlas of the normal intracranial electroencephalogram: Neurophysiological awake activity in different cortical areas. *Brain*, *141*(4), 1130–1144. https://doi.org/10.1093/brain/awy035

Freyer, F., Aquino, K., Robinson, P. A., Ritter, P., & Breakspear, M. (2009). Bistability and non-gaussian fluctuations in spontaneous cortical activity. *Journal of Neuroscience*, *29*(26), 8512–8524. https://doi.org/10.1523/JNEUROSCI.0754-09.2009

Freyer, F., Roberts, J. A., Becker, R., Robinson, P. A., Ritter, P., & Breakspear, M. (2011). Biophysical Mechanisms of Multistability in Resting-State Cortical Rhythms. *Journal of Neuroscience*, *31*(17), 6353–6361. https://doi.org/10.1523/JNEUROSCI.6693-10.2011

Freyer, F., Roberts, J. A., Ritter, P., & Breakspear, M. (2012). A Canonical Model of Multistability and Scale-Invariance in Biological Systems. *PLoS Computational Biology*, *8*(8), e1002634. https://doi.org/10.1371/journal.pcbi.1002634

Guimarães, D. A. (2021). Segmented Regression via the Shape Language Modeling for Multi-Slope Path-Loss Modeling. *Anais Do XXXIX Simpósio Brasileiro de Telecomunicações e Processamento de Sinais*. XXXIX Simpósio Brasileiro de Telecomunicações e Processamento de Sinais. https://doi.org/10.14209/sbrt.2021.1570730012

Haley, C. L., & Anitescu, M. (2017). Optimal bandwidth for multitaper spectrum estimation. *IEEE Signal Processing Letters*, *24*(11), 1696–1700. https://doi.org/10.1109/LSP.2017.2719943

He, H., & Thomson, D. J. (2010). Canonical bicoherence analysis of dynamic EEG data. *Journal of Computational Neuroscience*, *29*(1), 23–34. https://doi.org/10.1007/s10827-009-0177-z

Hinich, M. J. (1982). Testing for Gaussianity and Linearity of a Stationary Time Series. *Journal of Time Series Analysis*, *3*(3), 169–176. https://doi.org/10.1111/j.1467-9892.1982.tb00339.x

Hosking, J. R. M., & Wallis, J. R. (1997). *Regional Frequency Analysis: An Approach Based on L-Moments*. Cambridge University Press. https://doi.org/10.1017/CBO9780511529443

Hu, S., Zhang, Z., Zhang, X., Wu, X., & Valdes-Sosa, P. A. (2024). \bm\xi-\bm\pi: A nonparametric model for neural power spectra decomposition. *IEEE Journal of Biomedical and Health Informatics*, *28*(5), 2624–2635. IEEE Journal of Biomedical and Health Informatics. https://doi.org/10.1109/JBHI.2024.3364499

Hughes, A. M., Whitten, T. A., Caplan, J. B., & Dickson, C. T. (2012). BOSC: A better oscillation detection method, extracts both sustained and transient rhythms from rat hippocampal recordings. *Hippocampus*, *22*(6), 1417–1428. https://doi.org/10.1002/hipo.20979

Isaksson, A., Lagergren, K., & Wennberg, A. (1976). Visible and non-visible EEG changes demonstrated by spectral parameter analysis. *Electroencephalography and Clinical Neurophysiology*, *41*(3), 225–236. https://doi.org/10.1016/0013-4694(76)90116-4

Jing, X., & Lang, Z. (2015). *Frequency Domain Analysis and Design of Nonlinear Systems based on Volterra Series Expansion: A Parametric Characteristic Approach*. Springer International Publishing. https://doi.org/10.1007/978-3-319-12391-2

Jirsa, V., & Müller, V. (2013). Cross-frequency coupling in real and virtual brain networks. *Frontiers in Computational Neuroscience*, *7*. https://doi.org/10.3389/fncom.2013.00078

Klimesch, W. (2012). Alpha-band oscillations, attention, and controlled access to stored information. *Trends in Cognitive Sciences*, *16*(12), 606–617. https://doi.org/10.1016/j.tics.2012.10.007

Kosciessa, J. Q., Grandy, T. H., Garrett, D. D., & Werkle-Bergner, M. (2020). Single-trial characterization of neural rhythms: Potential and challenges. *NeuroImage*, *206*, 116331. https://doi.org/10.1016/j.neuroimage.2019.116331

Kramer, M. A., & Chu, C. J. (2024). A general, noise-driven mechanism for the 1/f-like behavior of neural field spectra. *Neural Computation*, *36*(8), 1643–1668. https://doi.org/10.1162/neco_a_01682

Labecki, M., Kus, R., Brzozowska, A., Stacewicz, T., Bhattacharya, B. S., & Suffczynski, P. (2016). Nonlinear Origin of SSVEP Spectra—A Combined Experimental and Modeling Study. *Frontiers in Computational Neuroscience*, *10*. https://doi.org/10.3389/fncom.2016.00129

Lackey, H. E., Sell, R. L., Nelson, G. L., Bryan, T. A., Lines, A. M., & Bryan, S. A. (2023). Practical guide to chemometric analysis of optical spectroscopic data. *Journal of Chemical Education*, *100*(7), 2608–2626. https://doi.org/10.1021/acs.jchemed.2c01112

Leonenko, N. N., Sikorskii, A. Y., & Terdik, G. (1998). *On spectral and bispectral estimator of the parameter of nongaussian data*. *6*(2), 159–182. https://doi.org/10.1515/rose.1998.6.2.159

Li, M., Wang, Y., Lopez-Naranjo, C., Reyes, R. C. G., Hamid, A. I. A., Evans, A. C., Savostyanov, A. N., Calzada-Reyes, A., Areces-Gonzalez, A., Villringer, A., Tobon-Quintero, C. A., Garcia-Agustin, D., Paz-Linares, D., Yao, D., Dong, L., Aubert-Vazquez, E., Reza, F., Omar, H., Abdullah, J. M., … Valdes-Sosa, P. A. (2022). Harmonized-Multinational qEEG Norms (HarMNqEEG). *NeuroImage*, 119190. https://doi.org/10.1016/j.neuroimage.2022.119190

Lindén, H., Pettersen, K. H., & Einevoll, G. T. (2010). Intrinsic dendritic filtering gives low-pass power spectra of local field potentials. *Journal of Computational Neuroscience*, *29*(3), 423–444. https://doi.org/10.1007/s10827-010-0245-4

Lopes da Silva, F. H., van Rotterdam, A., Barts, P., van Heusden, E., & Burr, W. (1976). Models of Neuronal Populations: The Basic Mechanisms of Rhythmicity. In M. A. Corner & D. F. Swaab (Eds.), *Progress in Brain Research* (Vol. 45, pp. 281–308). Elsevier. https://doi.org/10.1016/S0079-6123(08)60995-4

Marzocca, P., Nichols, J. M., Milanese, A., Seaver, M., & Trickey, S. (2008). Second-order spectra for quadratic nonlinear systems by Volterra functional series: Analytical description and numerical simulation. *Mechanical Systems and Signal Processing*, *22*, 1882–1895. https://doi.org/10.1016/j.ymssp.2008.02.002

McKeon, S. D., Perica, M. I., Parr, A. C., Calabro, F. J., Foran, W., Hetherington, H., Moon, C.-H., & Luna, B. (2024). Aperiodic EEG and 7T MRSI evidence for maturation of E/I balance supporting the development of working memory through adolescence. *Developmental Cognitive Neuroscience*, *66*, 101373. https://doi.org/10.1016/j.dcn.2024.101373

Mendoza-Halliday, D., Major, A. J., Lee, N., Lichtenfeld, M. J., Carlson, B., Mitchell, B., Meng, P. D., Xiong, Y. (Sophy), Westerberg, J. A., Jia, X., Johnston, K. D., Selvanayagam, J., Everling, S., Maier, A., Desimone, R., Miller, E. K., & Bastos, A. M. (2024). A ubiquitous spectrolaminar motif of local field potential power across the primate cortex. *Nature Neuroscience*, *27*(3), 547–560. https://doi.org/10.1038/s41593-023-01554-7

Mohsini, K. A., Farooq, O., Khan, Y. U., & Tripathi, M. (2017). Bispectral analysis of EEG during non-convulsive seizures. *2017 International Conference on Multimedia, Signal Processing and Communication Technologies (IMPACT)*, 209–213. https://doi.org/10.1109/MSPCT.2017.8364006

Narasimhan, S. V. (1989). Pole-zero spectral modeling of EEG. *Signal Processing*, *18*(1), 17–32. https://doi.org/10.1016/0165-1684(89)90059-5

Newville, M., Stensitzki, T., Allen, D. B., & Ingargiola, A. (2014). *LMFIT: Non-Linear Least-Square Minimization and Curve-Fitting for Python* (Version 0.8.0) [Computer software]. Zenodo. https://doi.org/10.5281/zenodo.11813

Nichols, J. M., Olson, C. C., Michalowicz, J. V., & Bucholtz, F. (2009). The Bispectrum and Bicoherence for Quadratically Nonlinear Systems Subject to Non-Gaussian Inputs. *IEEE Transactions on Signal Processing*, *57*(10), 3879–3890. IEEE Transactions on Signal Processing. https://doi.org/10.1109/TSP.2009.2024267

Nikias, C. L., & Mendel, J. M. (1993). Signal processing with higher-order spectra. *IEEE Signal Processing Magazine*, *10*(3), 10–37. https://doi.org/10.1109/79.221324

Nikias, C., & Petropulu, A. (1993). *Higher Order Spectra Analysis: A Non-Linear Signal Processing Framework* (Facsimile edition). Pearson.

Nozari, E., Bertolero, M. A., Stiso, J., Caciagli, L., Cornblath, E. J., He, X., Mahadevan, A. S., Pappas, G. J., & Bassett, D. S. (2024). Macroscopic resting-state brain dynamics are best described by linear models. *Nature Biomedical Engineering*, *8*(1), 68–84. https://doi.org/10.1038/s41551-023-01117-y

Pascual-Marqui, R. D., Kochi, K., & Kinoshita, T. (2022). *Cortical Xi-Alpha model for resting state electric neuronal activity* (No. arXiv:2212.13571). arXiv. https://doi.org/10.48550/arXiv.2212.13571

Pascual-marqui, R. D., Valdes-sosa, P. A., & Alvarez-amador, A. (1987). A Parametric Model for Multichannel EEG Spectra. *International Journal of Neuroscience*, *40*(1–2), 89–99. https://doi.org/10.3109/00207458808985730

Pascual-marqui, R. D., Valdes-sosa, P. A., & Alvarez-amador, A. (1988). A Parametric Model for Multichannel EEG Spectra. *International Journal of Neuroscience*, *40*(1–2), 89–99. https://doi.org/10.3109/00207458808985730

Peng, Z. K., Zhang, W. M., Yang, B. T., Meng, G., & Chu, F. L. (2013). The parametric characteristic of bispectrum for nonlinear systems subjected to Gaussian input. *Mechanical Systems and Signal Processing*, *36*(2), 456–470. https://doi.org/10.1016/j.ymssp.2012.10.010

Pfanzagl, J. (1969). On the measurability and consistency of minimum contrast estimates. *Metrika*, *14*(1), 249–272. https://doi.org/10.1007/BF02613654

Price-Whelan, A. M., Lim, P. L., Earl, N., & Others. (2022). The Astropy Project: Sustaining and Growing a Community-oriented Open-source Project and the Latest Major Release (v5.0) of the Core Package. *Astrophys. J.*, *935*(2), 167. INSPIRE. https://doi.org/10.3847/1538-4357/ac7c74

Raffaelli, G. T., Jiříček, S., & Hlinka, J. (2024). *Nonlinear brain connectivity from neurons to networks: Quantification, sources and localization* (p. 2024.11.17.623635). bioRxiv. https://doi.org/10.1101/2024.11.17.623635

Reyes, R. G., Gonzales, A. A., Wang, Y., Jin, Y., Minatti, L., & Valdes-Sosa, P. A. (2025). *Lifespan mapping of EEG source spectral dynamics with ξ − αNET* (p. 2025.02.21.639413). bioRxiv. https://doi.org/10.1101/2025.02.21.639413

Rice, J. (1979). On the estimation of the parameters of a power spectrum. *Journal of Multivariate Analysis*, *9*(3), 378–392. https://doi.org/10.1016/0047-259X(79)90095-2

Riedel, K. S., & Sidorenko, A. (1995). Minimum bias multiple taper spectral estimation. *IEEE Transactions on Signal Processing*, *43*(1), 188–195. IEEE Transactions on Signal Processing. https://doi.org/10.1109/78.365298

Roberts, J. A., & Robinson, P. A. (2012). Quantitative theory of driven nonlinear brain dynamics. *NeuroImage*, *62*(3), 1947–1955. https://doi.org/10.1016/j.neuroimage.2012.05.054

Sakhno, L. (2014). Minimum Contrast Method for Parameter Estimation in the Spectral Domain. In V. Korolyuk, N. Limnios, Y. Mishura, L. Sakhno, & G. Shevchenko (Eds.), *Modern Stochastics and Applications* (pp. 319–336). Springer International Publishing. https://doi.org/10.1007/978-3-319-03512-3_18

Sakhno, L. (2020). On the Estimation of Spectral Functionals of the Fourth Order for Stationary Random Fields. *Austrian Journal of Statistics*, *49*(4), 106–116. https://doi.org/10.17713/ajs.v49i4.1136

Seymour, R. A., Alexander, N., & Maguire, E. A. (2022). Robust estimation of 1/f activity improves oscillatory burst detection. *European Journal of Neuroscience*, *56*(10), 5836–5852. https://doi.org/10.1111/ejn.15829

Shahbazi Avarvand, F., Bartz, S., Andreou, C., Samek, W., Leicht, G., Mulert, C., Engel, A. K., & Nolte, G. (2018). Localizing bicoherence from EEG and MEG. *NeuroImage*, *174*(October 2017), 352–363. https://doi.org/10.1016/j.neuroimage.2018.01.044

Shahbazi, F., Ewald, A., & Nolte, G. (2014). Univariate normalization of bispectrum using Hölder's inequality. *Journal of Neuroscience Methods*, *233*, 177–186. https://doi.org/10.1016/j.jneumeth.2014.05.030

Sheremet, A., Burke, S. N., & Maurer, A. P. (2016). Movement Enhances the Nonlinearity of Hippocampal Theta. *Journal of Neuroscience*, *36*(15), 4218–4230. https://doi.org/10.1523/JNEUROSCI.3564-15.2016

Silva, L. R., Amitai, Y., & Connors, B. W. (1991). Intrinsic oscillations of neocortex generated by layer 5 pyramidal neurons. *Science*, *251*(4992), 432–435. https://doi.org/10.1126/science.1824881

Stark, J., Broomhead, D. S., Davies, M. E., & Huke, J. (1997). Takens embedding theorems for forced and stochastic systems. *Nonlinear Analysis: Theory Methods & Applications*, *30*(8), 5303–5314. https://doi.org/10.1016/S0362-546X(96)00149-6

Stiefel, K. M., & Ermentrout, G. B. (2016). Neurons as oscillators. *Journal of Neurophysiology*, *116*(6), 2950–2960. https://doi.org/10.1152/jn.00525.2015

Takens, F. (1985). On the numerical determination of the dimension of an attractor. In B. L. J. Braaksma, H. W. Broer, & F. Takens (Eds.), *Dynamical Systems and Bifurcations* (Vol. 1125, pp. 99–106). Springer Berlin Heidelberg. https://doi.org/10.1007/BFb0075637

Thomson, D. J. (1982). Spectrum estimation and harmonic analysis. *Proceedings of the IEEE*, *70*(9), 1055–1096. Proceedings of the IEEE. https://doi.org/10.1109/PROC.1982.12433

Thomson, D. J. (1989). Multi-window Bispectrum Estimates. *Workshop on Higher-Order Spectral Analysis*, 19–23. https://doi.org/10.1109/HOSA.1989.735263

Travert, A., & Fernandez, C. (2024). *SpectroChemPy* (Version 0.6.9) [Computer software]. Zenodo. https://doi.org/10.5281/ZENODO.3823841

Valdes, P. a, Jimenez, J. C., Riera, J., Biscay, R., & Ozaki, T. (1999). Nonlinear EEG analysis based on a neural mass model. *Biological Cybernetics*, *81*(5–6), 415–424.

Valdés, P., Bosch, J., Grave, R., Hernandez, J., Riera, J., Pascual, R., & Biscay, R. (1992). Frequency domain models of the EEG. *Brain Topography*, *4*(4), 309–319. https://doi.org/10.1007/BF01135568

Valdés-Sosa, P., Bosch, J., Jiménez, J., Trujillo-Barreto, N., Lirio, R. J., Morales, F., Hernandez Caceres, J. luis, & Ozaki, T. (1999). The statistical identification of nonlinear brain dynamics: A progress report. In *Non linear Dynamic and Brain Funcioning* (pp. 278–284).

Van Albada, S., & Robinson, P. (2013). Relationships between Electroencephalographic Spectral Peaks Across Frequency Bands. *Frontiers in Human Neuroscience*, *7*. https://www.frontiersin.org/articles/10.3389/fnhum.2013.00056

Van Kerkoerle, T., Self, M. W., Dagnino, B., Gariel-Mathis, M.-A., Poort, J., Van Der Togt, C., & Roelfsema, P. R. (2014). Alpha and gamma oscillations characterize feedback and feedforward processing in monkey

visual cortex. *Proceedings of the National Academy of Sciences*, *111*(40), 14332–14341. https://doi.org/10.1073/pnas.1402773111

Wang, Y., Li, M., Reyes, R. G., Ronaldo García Reyes, Bosch-Bayard, J., Bringas-Vega, M., Michael Breakspear, Minati, L., & Valdes-Sosa, P. (2025). Nonlinear properties of multistable states of intracranial EEG. *The Organization for Human Brain Mapping (OHBM) 2025 Annual Meeting*, 1339.

Wen, H., & Liu, Z. (2016). Separating Fractal and Oscillatory Components in the Power Spectrum of Neurophysiological Signal. *Brain Topography*, *29*(1), 13–26. https://doi.org/10.1007/s10548-015-0448-0

Wilson, L. E., da Silva Castanheira, J., & Baillet, S. (2022a). Time-resolved parameterization of aperiodic and periodic brain activity. *eLife*, *11*, e77348. https://doi.org/10.7554/eLife.77348

Wilson, L. E., da Silva Castanheira, J., & Baillet, S. (2022b). Time-resolved parameterization of aperiodic and periodic brain activity. *eLife*, *11*, e77348. https://doi.org/10.7554/eLife.77348

Zandvoort, C. S., & Nolte, G. (2021). Defining the filter parameters for phase-amplitude coupling from a bispectral point of view. *Journal of Neuroscience Methods*, *350*, 109032. https://doi.org/10.1016/j.jneumeth.2020.109032

Zetterberg, L. H. (1969). Estimation of parameters for a linear difference equation with application to EEG analysis. *Mathematical Biosciences*, *5*(3), 227–275. https://doi.org/10.1016/0025-5564(69)90044-3

Zhou, R., Yu, Y., & Li, C. (2024). Revealing neural dynamical structure of C. elegans with deep learning. *Iscience*, *27*(5). https://doi.org/10.1016/j.isci.2024.109759

Appendix

A.1 Mathematical notations

Table A 1 Basic mathematical symbols

Symbol	Definition
$x \in \mathbb{C}$ or $x \in \mathbb{C}$	Scalar
$\boldsymbol{x} \in \mathbb{C}^d$	Vector of size d (e.g., $\boldsymbol{x} = [x_i \vert i = 1, \cdots, d]$)
$\boldsymbol{X} \in \mathbb{C}^{d_1 \times d_2}$	Matrix of size $d_1 \times d_2$

Table A 2 Summary of indices

Symbol	Definition
i	Index of individual $i \in \{1, 2, \cdots N_i\}$, N_i is the total participants or subjects in the study
c	Index of the channel $c \in \{1, 2, \cdots, N_c\}$, N_c is total EEG channels
e	Index of EEG epochs $e \in \{1, 2, \cdots, N_e\}$, N_e is the disjoint segments selected from the continuous EEG
f	Physical frequencies with unit Hz
t	Physical time of each epoch
k	Index of taper, $k \in \{1, 2, \cdots, N_k\}$, where $N_k = 2NW - 1$
NW	Time-bandwidth product. N is the number of time samples in a single EEG epoch. W is the half-bandwidth of the tapers

Table A 3 Symbol of quantities and operators

Symbol	Name	Definition
$v_{i,c,e}(t) \in \mathbb{R}$ $v_{i,c,e}(f) \in \mathbb{C}$	EEG potential and its Discrete Fourier transform	EEG potential of the individual i, channel c of e-th epoch at a time t or frequency f for the Discrete Fourier transform.
$S_{i,c}(f) \in \mathbb{R}$	Theoretical spectra	The theoretical spectrum of an individual i channel c at the frequency f
$\widehat{S}_{i,c}(f) \in \mathbb{R}$	Power spectra	The empirical variance vector of $v_{i,c,e}(f)$ across all epochs for an individual i at the frequency f
$B_{i,c}(f_1, f_2) \in \mathbb{C}$	Theoretical Bispectrum	The theoretical bispectrum of an individual channel c at the bifrequency (f_1, f_2)
$\widehat{B}_{i,c}(f_1, f_2) \in \mathbb{C}$	Empirical Bispectrum	The empirical bispectrum of process $v_{i,c,e}(t)$ across all epochs for an individual i channel c at the bifrequency (f_1, f_2)

$b_{i,c}(f_1, f_2) \in \mathbb{C}$	Population Bicoherence	Population normalized bispectrum for individual i and channel c at the bifrequency (f_1, f_2)
$\hat{b}_{i,c}(f_1, f_2) \in \mathbb{C}$	Multitaper Bicoherence	Multitaper bicoherence estimator for individual i and channel c for bifrequency (f_1, f_2)
$\tilde{b}_{i,c}(f_1, f_2) \in \mathbb{C}$	BisCA Bicoherence	BiSCA -model estimator for individual i and channel c for bifrequency (f_1, f_2)
$\mathrm{E}[\cdot]$	Expectation	The expectation of a random variable
$\mathrm{Var}[\cdot]$	Variance	The variance of a random variable
$[\cdot]^*$	Complex conjugate	The complex conjugate of a variable

A.2 Summary of EEG Spectral Parameterization Methods

As a typical machine learning problem, many toolboxes implemented the curve fitting for spectroscopic data analysis — such as SpectroChemPy (Travert & Fernandez, 2024), PNNL Chemometric Toolbox(Lackey et al., 2023) astronomy data.modeling (Price-Whelan et al., 2022), SLM (Shape Language Modeling) (Guimarães, 2021), LMFIT (Levenberg-Marquardt least-squares minimization)(Newville et al., 2014). This paper emphasizes studies that have been applied specifically to EEG spectral analysis with certain constraints of biophysical prior.

Table A 4 Summary of EEG Spectral Parameterization Methods

Method	Feature	Citation
SPA (Spectral Parameter Analysis)	Calculate the resonance peaks information from the poles and zeros of the autoregressive model	(Isaksson et al., 1976; Narasimhan, 1989; Zetterberg, 1969)
Xi-Alpha (ξα)	Additive t-student kernels in nature scale fitted with maximum Whittle's likelihood	(Pascual-marqui et al., 1987)
BOSC (Better Oscillation Detection)	Thresholds for time and amplitude to detect and parametrize the burst of rhythm in time frequency	(Hughes et al., 2012; Kosciessa et al., 2020; Seymour et al., 2022)

Gaussian peak fit	Least square Gaussian peak fit	(Van Albada & Robinson, 2013)
IRASA (Irregular-Resampling Auto-Spectral Analysis)	Resampling to shift the spectra and using a media curve to get components	(Wen & Liu 2016)
SpecParam (Spectral parameterization) or FOOOF (Fitting Oscillations & One Over F)	Sequentially fit peaks through least square Gaussian fit in the log-scale	(Donoghue et al., 2020)
SPRiNT (Spectral Parameterization Resolved in Time)	Parametrize the peaks in the smoothed short-time Fourier transforms	(Wilson et al., 2022b)
PaWNextra (Pink and White Noise extraction)	Least square fit	(Barry & Blasio, 2021)
Cortical Xi-Alpha	Nonnegative matrix decomposition for multichannel	(Pascual-Marqui et al., 2022)
Xi-Pi (ξ-π)	Fit nonparametric spectrum components with Whittle's likelihood	(Hu et al., 2024)
Xi-Alpha Net	Hierarchical Bayesian model for solving the State space model with Xi-Alpha prior to reconstruct the source space spectrum	(Reyes et al., 2025)
BiSCA (Higher-order Xi-Alpha Model)	Parametrize both spectrum and bispectrum with joint likelihood	This paper

A.3 Gaussianity and Linearity test through the bicoherence

The original Hinich test for Gaussianity and linearity relies on the sum of squared bicoherence values, which can be highly sensitive to large bicoherence values arising from concentrated nonlinear interactions, such as narrow-band phase coupling. This sensitivity can lead to rejection of the null hypothesis even when the data exhibits localized nonlinearity rather than widespread non-Gaussianity, potentially causing false positives in Gaussianity tests. Specifically, the sum-based test suffers from extreme values introduced by the nonlinearity of the process or system, which can dominate the statistic and misrepresent the overall distribution as non-Gaussian.

For linearity, traditional tests based on the interquartile range (IQR) of bicoherence values are less effective. The IQR, being a measure of statistical dispersion focused on the middle 50% of the data, is insensitive to narrow-band quadratic phase coupling. These effects manifest as sparse extreme values that do not significantly influence the IQR, leading to a loss of power in detecting isolated peaks, which are critical for identifying localized nonlinearities. This insensitivity reduces the test's ability to capture significant nonlinear interactions that are not centrally distributed.

These tests enhance the original Hinich framework by targeting distinct aspects of deviation from the null hypothesis. The median-based test offers a robust assessment of Gaussianity by focusing on central tendency, while the maximum-based test isolates strong nonlinear interactions. Both leverage bicoherence's ability to measure quadratic phase coupling, with their statistical properties validated through theoretical derivations and simulations.

A.3.1 Gaussianity test: Median-Based Test Derivation

Under the null hypothesis of Gaussianity and linearity, for each frequency pair (f_1, f_2), the squared bicoherence scales as:

$$2N_s|b(f_1,f_2)|^2 \sim \chi^2(2)$$

Thus, $|b(f_1,f_2)|^2 \sim \frac{1}{2N_s}\chi^2(2)$. The population median of a $\chi^2(2)$ distribution is $2\ln 2 \approx 1.386$, so the median of $|b(f_1,f_2)|^2$ is $\frac{\ln 2}{N_s}$. The expected value of the test statistic is:

$$E[t_{\text{median}}] \approx 2N_s \cdot \frac{\ln 2}{N_s} = 2\ln 2$$

For a large number of frequency pairs P, the sample median is asymptotically normal. The probability density function (PDF) of $|b(f_1, f_2)|^2$ is:

$$f(x) = N_s e^{-N_s x}$$

At the median $\mu = \frac{\ln 2}{N_s}$, $f(\mu) = \frac{N_s}{2}$. The asymptotic variance of the sample median is:

$$\text{Var}(t_{\text{median}}) = \frac{1}{4Pf(\mu)^2} = \frac{1}{PN_s^2}$$

Thus, the variance of $t_{\text{median}} = 2N_s \cdot \text{median}_{f_1, f_2}\{|b(f_1, f_2)|^2\}$ is:

$$\text{Var}(t_{\text{median}}) = (2N_s)^2 \cdot \frac{1}{PN_s^2} = \frac{4}{P}$$

Therefore, the test statistic follows:

$$t_{\text{median}} \sim \mathcal{N}\left(2\ln 2, \sqrt{\frac{4}{P}}\right)$$

A.3.2 Linearity test: Maximum-Based Test Derivation

For the maximum-based test, we account for non-Gaussianity by estimating the non-centrality parameter λ_0:

$$\hat{\lambda}_0 = \max(\text{median}_{f_1, f_2}\{2N_s|b(f_1, f_2)|^2\} - 2, 0)$$

This reflects that the mean of a non-central $\chi^2(2, \lambda_0)$ distribution is $2 + \lambda_0$, with the median approximately $2\ln 2 + \lambda_0$ for small λ_0. Using extreme value theory (EVT), the maximum of P independent and identically distributed $\chi^2(2, \lambda_0)$ variables is approximated by a Gumbel distribution. The normalizing constants are:

- $b_P = F^{-1}(1 - 1/P)$, the value where the cumulative distribution function (CDF) F of $\chi^2(2, \lambda_0)$ reaches $1 - 1/P$,

- $a_P = \frac{1}{Pf(b_P)}$, where f is the PDF of $\chi^2(2, \lambda_0)$.

Thus, the test statistics are as follows:

$$t_{\max} \sim \mathrm{Gumbel}(b_P, a_P)$$

These derivations provide the theoretical foundation for applying the tests in practice, ensuring robust detection of deviations from Gaussianity and linearity.

A.3.3 Effective number segments estimate

Multitaper spectral methods and overlapping segments increase the N_s in bicoherence estimation but still dependencies between segments, reducing the effective number of independent samples (N_s^{eff}) compared to the nominal N_s. This affects the scaling of bicoherence statistics, where $2N_s|b(f_1, f_2)|^2 \sim \chi^2(2)$ under the null hypothesis. Using the nominal N_s can lead to incorrect p-values and thresholds. We estimate N_s^{eff} as follows:

1. Fit an autoregressive (AR) model to the time series $x(t)$ using the Burg method, selecting the best order with AICc (Corrected Akaike Information Criterion);

2. Generate M simulated time series using the AR model with Gaussian innovations, matching the length N of the observed data, in this paper $M = 100$, $N = 12000$;

3. Compute bicoherence $b(f_1, f_2)$ for each simulated series using the same parameters (multitaper method, window, FFT length, overlap, Haubrich normalization);

4. Calculate the mean value of squared bicoherence magnitudes:

$$\mathrm{mean}(|b(f_1, f_2)|^2) = \frac{1}{P} \sum_{f_1, f_2} |b(f_1, f_2)|^2,$$

where P is the number of valid frequency pairs;

5. Estimate N_s^{eff} as:

$$N_s^{\text{eff}} = \frac{1}{\text{mean}(|b(f_1, f_2)|^2)}.$$

The estimated N_s^{eff} accounts for dependencies from multitaper methods (via time-bandwidth product NW) and segment overlap, ensuring accurate scaling of test statistics for bicoherence-based Gaussianity and linearity tests.

A.4 Simulation

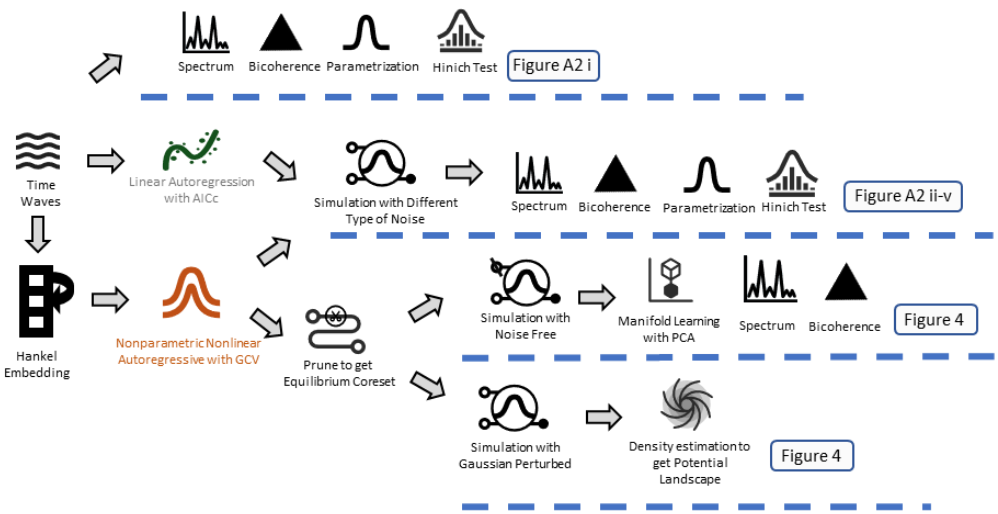

Figure A 1 Flowchart of the Simulation and Analysis Pipeline. *This diagram illustrates the methodology for analyzing real intracranial EEG (iEEG) data and generating four corresponding types of synthetic surrogate data to test for nonlinearity and non-Gaussianity, also the demonstration graph in figure 4. (1) Direct Analysis of Real Data (Top Path, Ref: Figure A2 i): The process begins with a real iEEG time series. This signal is directly subjected to spectral and bispectral analysis to compute its empirical power spectrum and bicoherence, establishing a real-data baseline. (2) Linear and Nonlinear Surrogate Generation (Middle Path, Ref: Figure A2 ii-v): A linear Autoregressive (AR) and a Nonparametric Nonlinear Autoregressive (NNAR) model is fitted to the real iEEG data. The optimal model order is selected using the Akaike Information Criterion corrected (AICc). This AR model and NNAR model are then used to generate two types of time series by driving it with different stochastic innovations: Linear/Nonlinear Gaussian: Using Gaussian (normal) distributed noise. Linear/Nonlinear Non-Gaussian: Using skewed, non-Gaussian noise (Pearson Type III distribution). (3). Simulation demonstration of the bicoherence and time domain Geometric for the Figure 4: after fitting the NNAR model to the real data, only the states close to the equilibrium is be maintained in the model and used to simulate to get spectrum, bicoherence and 2d embedded potential (density) function.*

A.4.1 Simulation for the Hinich's test and ENPSC parametrization demonstration

Here is an example of our bicoherence analysis for different types of signals, we put a simulation demonstration consisting of one channel of real data and 4 corresponding synthetic data (linear Gaussian, linear non-gaussian, nonlinear Gaussian, and nonlinear non-gaussian).

1. Real data: one channel from the MNI atlas data, with Fs=200 and 12000 time points samples.

2. Linear Gaussian process: This simulation used an Autoregressive (AR) model with Gaussian innovation.

$$\tilde{x}_{t+1} = \sum_{i=0}^{p-1} \hat{a}_i \tilde{x}_{t-i} + \tilde{u}_t (t = p, ..., N + p - 1) \tag{17}$$

The AR coefficient is fitted with the real data using Burg's method. In this example, a 45-order AR model is selected with AICc criteria, and the innovation is $N(0,1)$. We simulated $N = 12000$ samples with this AR model, also the same length for the rest 3 simulations.

3. Linear non-gaussian process: Instead of using the Gaussian innovation, here we use the Pearson type III distribution(Hosking & Wallis, 1997) as the innovation enables us to control the first to third-order moment for the distribution. The probability density function is

$$f(u) = \begin{cases} \dfrac{(u-\xi)^{\alpha-1} e^{-(u-\xi)/\beta}}{\beta^{\alpha}\Gamma(\alpha)}, \ \gamma > 0 \\ \dfrac{1}{\sqrt{2\pi}} e^{-\frac{1}{2}\left(\frac{u-\mu}{\sigma}\right)^2}, \ \gamma = 0 \\ \dfrac{(u-\xi)^{\alpha-1} e^{-(\xi-u)/\beta}}{\beta^{\alpha}\Gamma(\alpha)}, \ \gamma < 0 \end{cases} \tag{18}$$

where the parameter of the distribution $\alpha = 4/\gamma^2$, $\beta = \frac{1}{2}\sigma|\gamma|$ and $\xi = \mu - 2\sigma/\gamma$. The parameter μ is the center of distribution, σ is the standard deviation, γ is the skewness. Here we take $\mu = 0$, $\sigma = 1$ and $\gamma = 10$.

4. Nonlinear Gaussian process: Instead of linear p-lag AR model in the linear case, here we used a nonparametric nonlinear autoregressive (NNAR) model to fit the data (Valdés-Sosa et al., 1999), and simulate 12000 timepoints data recursively. Given timeseries $\{x_t\}_{t=1}^{N_t}$, reconstruct phase space via delay embedding:

$$\boldsymbol{x}_t = [x_t, x_{t-1}, ..., x_{t-p+1}]^T \in \mathbb{R}^p \tag{19}$$

The state evolution is modeled as the discrete nonlinear state space model

$$\tilde{\boldsymbol{x}}_{t+1} = F(\tilde{\boldsymbol{x}}_t) + \tilde{\boldsymbol{u}}_t \tag{20}$$

where $F(\cdot):\mathbb{R}^p \to \mathbb{R}^p$ is a p dimensional nonparametric function estimated via adaptive local constant regression (Nadaraya-Waston regression). To simplify the notation to fit regression notation, define embedding vector keys set $\{\boldsymbol{x}_k, \boldsymbol{y}_k\}_{k=1}^{n}$ stored all observed data with $\boldsymbol{x}_k = \boldsymbol{x}_t$ and $\boldsymbol{y}_k = \boldsymbol{x}_{t+1}$, $n = N_t - p - 1$.

$$\hat{F}(\boldsymbol{x}_q^*) = \frac{\sum_{k=1}^{n} K_{h_k}(\boldsymbol{x}_k, \tilde{\boldsymbol{x}}_q)\boldsymbol{y}_k}{\sum_{k=1}^{n} K_{h_k}(\boldsymbol{x}_k, \tilde{\boldsymbol{x}}_q)} \tag{21}$$

$\tilde{\boldsymbol{x}}_q$ is the query vector state during the N-step forward forecasting. The local weights are calculated by the kernel distance $K_{h_k}(\boldsymbol{x}_k, \boldsymbol{x}_q) = \exp\left(-\frac{\| \boldsymbol{x}_k - \boldsymbol{x}_q \|^2}{2h_k^2}\right)$ with bandwidth h_k. The h_k is the hyper parameter of model, in order to handle non-uniform distribution of the states in the p dimension space, we use the κ-th nearest neighborhood $\boldsymbol{x}_{[k,\kappa]}$ of each $\boldsymbol{x}_k$ to determine the local bandwidth

$$h_k = \frac{\| \boldsymbol{x}_{[k,\kappa]} - \boldsymbol{x}_k \|}{\sqrt{p}} \tag{22}$$

To select κ, this paper used a generalized cross-validation (GCV) on the real data $\{x_t\}_{t=1}^{N}$ from case 1, to find the best κ of and record the corresponding h_k for each states $\boldsymbol{x}_k$ in the one-step forward prediction task.

$$\mathrm{GCV}(\kappa) = \frac{\mathrm{MSE}(\kappa)}{(1 - \mathrm{tr}(\boldsymbol{L}(\kappa))/n)^2}$$

where the smoother matrix with elements

$$L_{k,q}(\kappa) = \frac{K_{h_k}(\boldsymbol{x}_k, \boldsymbol{x}_q)}{\sum_{k=1}^{n-1} K_{h_k}(\boldsymbol{x}_k, \boldsymbol{x}_q)}$$

To be computationally efficient, here we use scalar h_k, bandwidth is equal for all dimensions. The embedding dimensions p are used the same as linear simulation case 2 and case 3. The

nonparametric function $\hat{F}(\cdot)$ represent all the information of the original (Hankel embedded) state space or the differential manifold of the system, therefore, we didn't update this nonparametric function during evolution. In the simulation the innovation $\boldsymbol{u}_t^*$ is a multivariable gaussian distribution $\boldsymbol{z}_t$ and scaled with covariance from the residual of the one-step forward prediction $\boldsymbol{u}_t^* = \boldsymbol{L}\boldsymbol{z}_t$, where $\boldsymbol{L}$ is the Cholesky of the covariance matrix of the residual $\boldsymbol{L}\boldsymbol{L}^T = \boldsymbol{\Sigma}$, and $\boldsymbol{\Sigma} = \frac{1}{n-1}\boldsymbol{\epsilon}^T\boldsymbol{\epsilon} + \lambda \boldsymbol{I}_p$ with $\boldsymbol{\epsilon} = \boldsymbol{X} - \hat{\boldsymbol{X}} = [\epsilon_{t,1}, \epsilon_{t,2}, \ldots, \epsilon_{t,p}]_{t=1}^n$.

5. Nonlinear non-gaussian process: The nonlinear system follows the configuration of case 4. Instead of Gaussian innovation, we use Pearson type III (18) to generate the innovation $\boldsymbol{z}_t$ and then the $\boldsymbol{u}_t^*$.

All 5 cases apply the Multitaper estimation and the BiSCA model fitting with the same parameters as the analysis for real data.

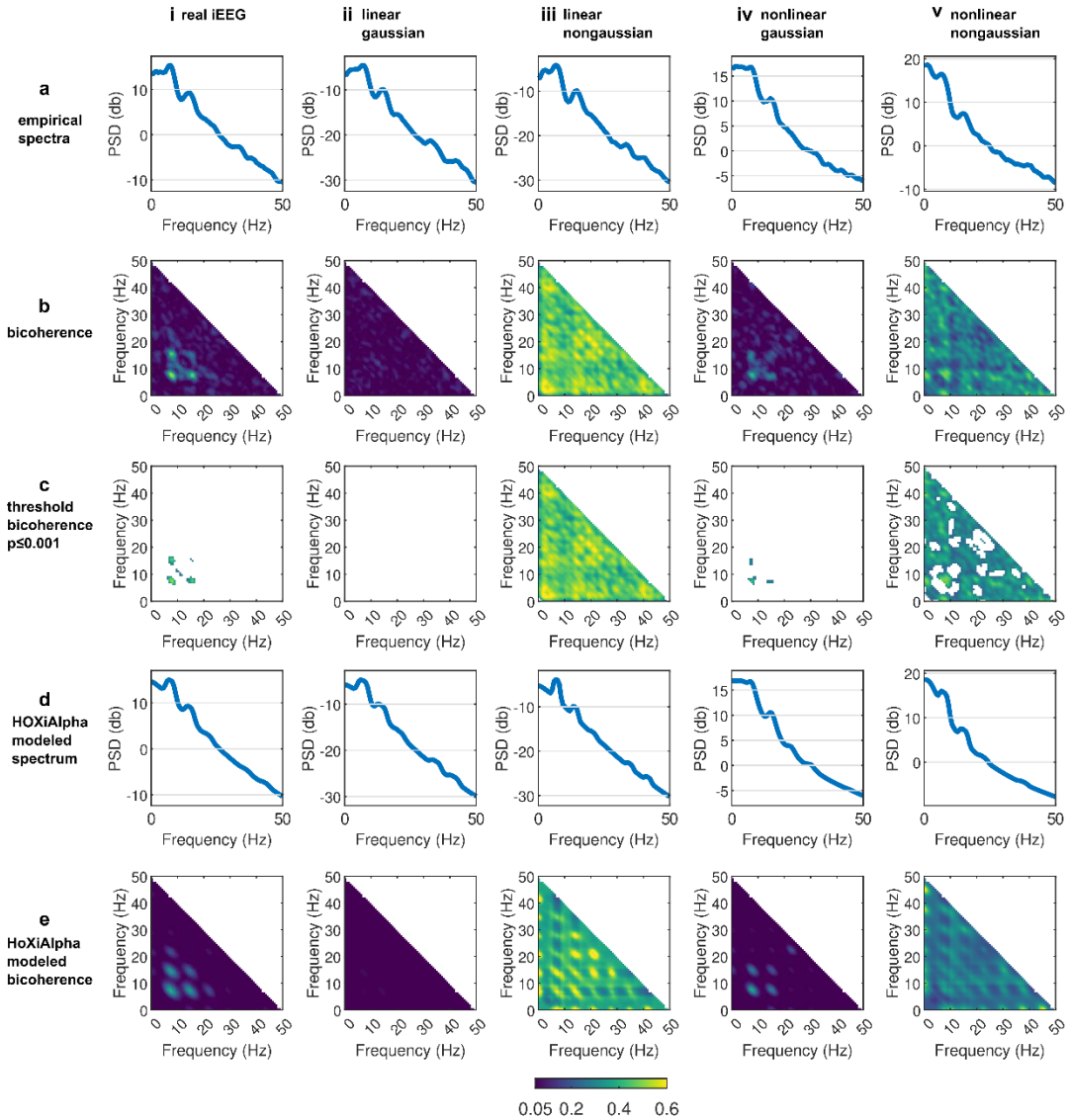

Figure A 2 Simulation demonstration. *Column from left to right are the 5 cases described in the simulation (i) real iEEG of MNI atlas data; (ii) linear Gaussian; (iii) linear non-Gaussian ; (iv) nonlinear Gaussian; (v) nonlinear non-Gaussian; Row from top to bottom is the result of analysis of each step (a) empirical spectrum calculated with Multitaper method; b) empirical modulus bicoherence calculated with Multitaper method with color scale indicating bicoherence modulus amplitude.; (c) threshold bicoherence with parametric test of p≤0.001: providing a clearer view of which frequency interactions are nonlinearly coupled beyond test level; (d) the spectrum from the fitted BiSCA model; (e) the bicoherence from the fitted BiSCA model: illustrating how well the model captures the observed nonlinear/non-Gaussian dynamics*

Figure A 2 illustrates how non-Gaussianity and nonlinearity impact neural time series analyses; we synthesized intracranial EEG (iEEG) signals under five distinct scenarios—real iEEG data (MNI atlas), linear Gaussian, linear non-Gaussian, nonlinear Gaussian, and nonlinear non-Gaussian—and compared their power spectrum and bicoherence pattern. The real iEEG data Figure A 2i exhibits a characteristic

1/f-like power spectrum with modest but significant bicoherence clusters after thresholding ($p \leq 0.001$). This empirical baseline reveals that genuine neural signals naturally contain nonlinear and Gaussian features.

In the Figure A 3 we show the result of statistic test of Figure A 2. Real iEEG (Top-Left): Both tests are significant, indicating the presence of both nonlinear interactions and non-Gaussian characteristics in the neural data. Linear Gaussian (Middle-Left): As expected for the null case, neither test is significant, correctly identifying the signal as linear and Gaussian. Linear Non-Gaussian (Middle-Right): Only the Gaussian test is significant, demonstrating the method's ability to isolate non-Gaussian properties in the absence of nonlinearity. Nonlinear Gaussian (Bottom-Left): Only the linear test is significant, successfully detecting nonlinear dynamics driven by Gaussian innovations. Nonlinear Non-Gaussian (Bottom-Right): Both tests are significant, correctly identifying the joint presence of nonlinearity and non-Gaussianity. Overall, this figure demonstrates how the combined use of maximum and median bicoherence statistics provides a robust framework for disentangling the distinct contributions of nonlinearity and non-Gaussianity in complex time series. Results Interpretation:

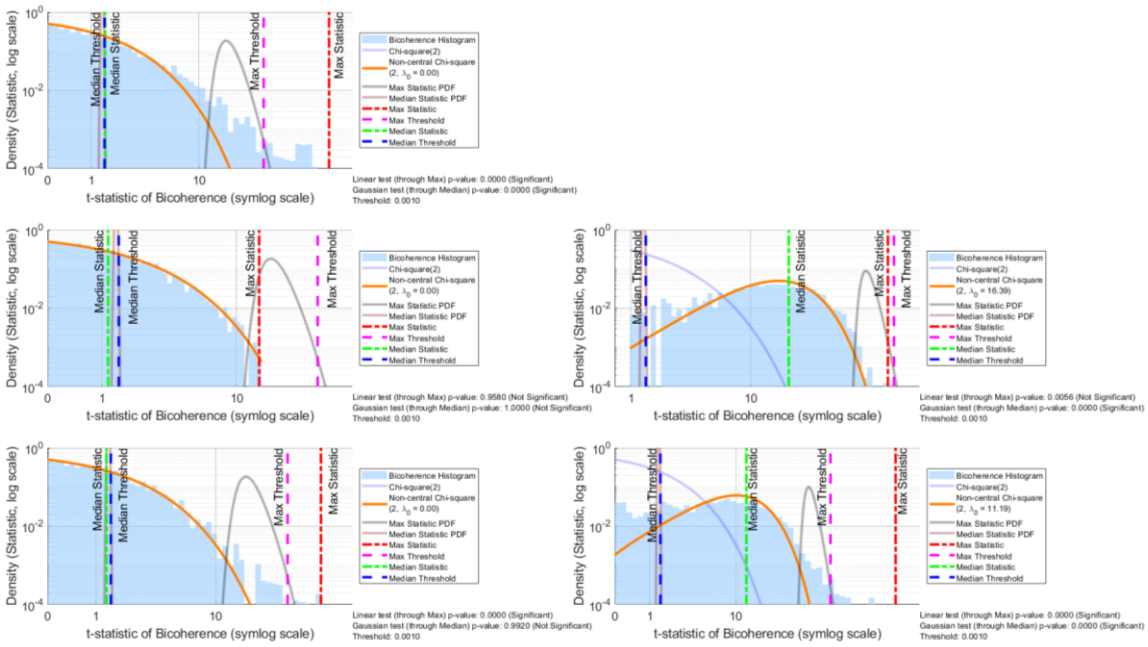

Figure A 3: Statistical analysis of bicoherence for real and simulated time series. *The figure displays the results of statistical tests applied to the bicoherence of five different time series signals to distinguish between nonlinearity and non-Gaussianity. The five cases are: (Top-left) Real intracranial EEG (iEEG) data; (Middle-left) A simulated linear Gaussian process; (Middle-right) A*

simulated linear non-Gaussian process; (Bottom-left) A simulated nonlinear Gaussian process; and (Bottom-right) A simulated nonlinear non-Gaussian process. Each subplot shows: Bicoherence Histogram (Light Blue): The distribution of the t-statistic calculated from the empirical bicoherence values of the signal. Chi-square Distributions: The theoretical central chi-square distribution with 2 degrees of freedom (blue line, $\chi^2(2)$), which is expected for a linear Gaussian process. A non-central chi-square distribution (orange line) is fitted to the data, where the non-centrality parameter (λ_0) captures deviations from the null hypothesis, related to non-Gaussianity. Statistic PDFs (Gray and Dark Red): The probability density functions for the 'Max' and 'Median' statistics, representing the expected distribution under the null hypothesis. Vertical Lines: The observed values for the 'Max Statistic' (red) and 'Median Statistic' (green) are compared against their respective significance thresholds, 'Max Threshold' (magenta) and 'Median Threshold' (blue). The text at the bottom of each plot summarizes two hypothesis tests: 1. Linear test (through Max): Uses the maximum bicoherence value to test for significant quadratic phase coupling, which indicates nonlinearity. A significant result occurs if the 'Max Statistic' exceeds the 'Max Threshold'. 2. Gaussian test (through median): Uses the median bicoherence value to test for a constant offset in bicoherence, which is characteristic of linear non-Gaussian processes. A significant result occurs if the 'Median Statistic' exceeds the 'Median Threshold'.

The result shows that the bicoherence can be different even if the second-order spectrum is similar. In the linear non-Gaussian scenario Figure A 2 ii, the data deviate from Gaussianity but do not exhibit intrinsic nonlinear dependencies. According to (8), this linear yet non-Gaussian structure typically manifests as a uniform or "constant" offset in the bicoherence. In other words, rather than showing localized peaks at specific bifrequencies, the bicoherence tends to exhibit a more diffuse elevation across the entire frequency domain. Conversely, the bicoherence in the nonlinear Gaussian scenario is limited to well-defined regions (i.e., specific bifrequencies where nonlinearity introduces phase coupling), with otherwise negligible values. This difference underscores that nonlinearity and non-Gaussianity can contribute distinctly to the observed cross-frequency coupling patterns, helping to explain why the bicoherence in the linear non-Gaussian simulation diverges markedly from that of real iEEG data.

We further fitted each case with our BiSCA model, which accurately reproduced both the power spectral density and bicoherence for each scenario (rows of *d* and *e* in Figure A 2). Notably, the model faithfully recapitulated the real iEEG features, mirroring the 1/f-like spectral decay and the subtle, significant cross-frequency interactions. These results highlight the model's capacity to disentangle and reconstruct complex neural signals, shedding light on the interplay of Gaussianity and nonlinearity that shapes iEEG dynamics.

A.4.2 Simulation for the Geometric view of bicoherence

The simulation of Figure 4 shown the geometric point of view of the bicoherence. The simulation employed a NNAR method to analyze nonlinear dynamics in intracranial iEEG data containing Wicket . The pipeline began with preprocessing a 2-second iEEG segment (sampled at 200 Hz) from a subject with normal variant activity. After reconstructing the phase space using a 23rd-order embedding, the NNAR

model was trained to capture the system's dynamics. A pruning step removed non-equilibrium states, retaining only key dynamics with weighted contributions exceeding 1e-2.

$$\mathcal{S} = \left\{ \boldsymbol{x}_k \mid \sum_{q=1}^{n_{eq}} w_k^{(q)} > \tau \right\}, \quad w_k^{(q)} = K_{h_k}(\| \boldsymbol{x}_k - \boldsymbol{x}_q^{eq} \|)$$

Deterministic and stochastic forecasts were generated using the pruned model. The deterministic (noise free) simulation to show the 3D phase portrait skeleton visualization, spectrum and bicoherence of this limit cycle. The stochastic forecasts with innovations modeled as Gaussian noise scaled by residual covariance to obtain potential landscape of 2D state space. The system's geometry was projected into 2D/3D state spaces via PCA of the high dimensional states set $\mathcal{S}$, and potential landscapes were estimated using kernel density methods on 100×100 grids, this is a nonparametric version of the landscape estimation R. Zhou et al., (2024). Spectrum and bicoherence, was implemented also with multitaper estimators ($NW = 2.5$) across 300-sample windows with 75% overlap.

To contrast with the asymmetric dynamics, we simulated symmetric nonlinear oscillations by enforcing the nonparametric state evolution function to satisfy $F(-\boldsymbol{x}) = -F(\boldsymbol{x})$,making the system dynamics invariant under state inversion $(\mathbf{X} \to -\mathbf{X})$. The modified state evolution becomes:

$$\tilde{\boldsymbol{x}}_{t+1} = \frac{F(\tilde{\boldsymbol{x}}_t) - F(-\tilde{\boldsymbol{x}}_t)}{2} + \tilde{\boldsymbol{u}}_t,$$

where the averaging ensures cancellation of even-order nonlinearities.

The reconstructed phase portrait revealed a stable limit cycle (Figure 4c), confirming the system's oscillatory nature. The potential landscape exhibited asymmetric minima (Figure 4d), explaining the spikes' directional morphology. Spectral analysis showed harmonically related peaks at 8.7Hz and 17.4Hz (Figure 4e), with total harmonic distortion (THD) -4.08dB. Bicoherence analysis demonstrated significant phase coupling between fundamental and harmonic components (Figure 4f), quantifying the nonlinear interactions. The symmetric version of the system, depicted in subplot (g) to (k), provides a contrasting perspective to the asymmetric case. Besides the symmetricity of the time domain analysis (g) to (i), the spectrum shows it only has the odd order harmonics, therefore, the bicoherence shows zero everywhere.

The asymmetric bicoherence profile (Figure 4f) reflects directionally biased nonlinear interactions, characteristic of depolarization-hyperpolarization asymmetry in the neuronal networks. The reconstructed limit cycle (Figure 4c) suggests possible self-sustaining oscillations stabilized by voltage-gated ion channel dynamics during the sample time interval. The potential landscape's asymmetry (Figure 4) aligns with the greater energy required for spike initiation versus termination, consistent with sodium channel inactivation kinetics. The 9 Hz spectral peak corresponds to thalamocortical resonance frequencies implicated in spike-wave generation. While the model successfully captured short-term dynamics (τ < 100 ms), longer simulations showed phase drift, this could be introduced by the step of pruning removed the activities shifted by the slow variables, the underlying attractor may not perfect limit cycle but quasiperiodic or chaotic, suggesting the need for additional slow variables in future extensions (Stiefel & Ermentrout, 2016; Breakspear, 2017). These analysis bridges the spectral domain nonlinear analysis with the time domain evolution, providing a framework for quantifying stability landscapes in the nonlinear oscillations

A.5 Goodness of fit

To demonstrate how much variance can be explained by the model, here we put the cumulative density function of the R^2. In the formula defined in (14) and (16), the parameter $\{\mu_{\rho,k}\}$ has two options: 1) Harmonic fixed with the harmonic relationship of the "fundamental oscillation", 2) Free: initialize with spectrum and optimize the joint fit. We put the R^2 of both cases here.

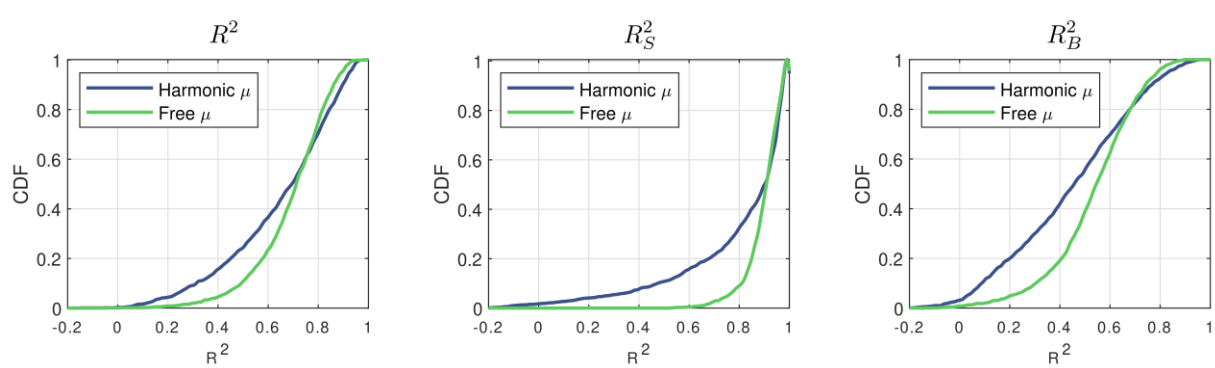

Figure A 4 Distributions of the coefficient of determination R^2 in three different conditions. *a) is the R^2 of the full model; b) is the R^2 for the spectrum; c) is the R^2 for the bispectrum*

The R^2 distribution is calculated for the fit of each channel shown in the Figure A 4. The goodness of fit suggests that the model's goodness of fit varies considerably across the entire dataset. The "free" option of the peak center fits with a greater degree of freedom. Therefore, its R^2 is concentrated on the right side, compared to the "harmonic" organized center peak option. Some phenomena, such as split Alpha, may not be described by the "harmonic" organized model.

Figure A 4 (a) shows a broad distribution of overall R^2 values, suggesting that the model's goodness of fit varies considerably across the entire dataset. A noticeable upward trend toward higher R^2 (up to ≈ 1) indicates that many data segments exhibit strong fits, although a small portion remains at the lower end of the scale. Since the variance of the spectrum and the variance of the bispectrum is quite different, which also vary with subject the R_S^2 and R_B^2 are more intuitive. Figure A 4 (b) R_S^2 are comparatively narrower near the high value but rise sharply toward $R_S^2 \approx 1$. This pattern implies that many single-subject spectral fits are quite robust, with fewer cases in the middle range of goodness of fit. Figure A 4 (c) presents a more bell-shaped distribution of baseline R_B^2 values. Most of these are clustered around moderate goodness-of-fit levels $R_B^2 \approx 0.4–0.6$, with fewer instances at the extremes (near 0 or near 1). Overall, bispectrum fits appear to be consistent but rarely reach near-perfect levels.

A.6 Peak relation from the spectrum

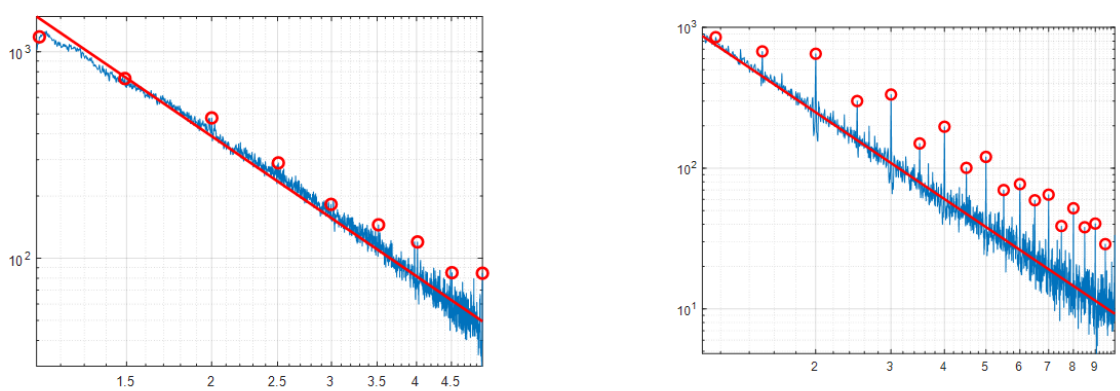

Figure A 5 the ratio of the peaks identified in the spectrum. *The left is from harmonized 1563 × 18 channels scalp EEG data. The right is from 1771 channels of iEEG data.*

Besides integer harmonic peaks of periodic oscillations, other proportions between peak frequency reveal possible quasi-periodic motion and chaotic; the distribution of the proportions showed possible scale free of the organization of peaks. On the Exponent Scale, the slope is 2.2531 for EEG and 2.0493 for iEEG. However, metaphysical models attempt to impose intriguing physical interpretations on empirical data without necessarily ensuring that these interpretations adhere to rigorous statistical or biophysical validity. Evertz et al. (2022) point out correctly that there is doubt that the aperiodic component is either "scale-free" or a reflection of criticality. An alternative is to look at biophysical models with effects of the extracellular space (Lindén et al., 2010) as mentioned by Evertz et al. (2022). In addition to interest and questions about the scale-free nature of ξ process (Bédard et al., 2006). This question was discussed in Valdés-Sosa et al. (1999) and Valdes-Sosa et al. (1999), when people argue that the EEG is chaos, the neural activity is a nonlinear stochastic system driven by the noise. We reserve these possibilities, and these conclusions still need to be verified by rigorous statistical methods. One possibility is that using the bicoherence in this paper to study the relationship between the components is possible when all the ratios here are the intermodulation combination of the integer peaks.